Department of Physics and Astronomy

Heidelberg University

Bachelor Thesis in Physics

submitted by

Sophie Armbruster

born in Frankfurt am Main (Germany)

2021

Cryogenic ^{222}Rn detector

This Bachelor Thesis has been carried out by Sophie Armbruster at the
Max Planck Institute for Nuclear Physics in Heidelberg
under the supervision of
Prof. Dr. Dr. h.c. Manfred Lindner

Abstract

Last century our understanding of the laws that govern nature developed astonishingly. Still, several mysteries remain unsolved e.g. the origin of neutrino masses, the particle-nature of neutrinos and the potential existence of dark matter particles. Current world-leading experiment sensitivities are being limited by self-induced backgrounds. In particular the XENONnT experiment which aims to discover dark matter in form of weakly interacting massive particles (WIMPs) is impaired by radon emanation from its detector materials. A very successful strategy to mitigate ^{222}Rn emanation from detector materials is to select or treat for radon-clean materials used to build the detector. Large automatized ^{222}Rn screening facilities are hence crucial to study and monitor the different levels of radon emanation. There are many different ^{222}Rn detectors available. They differ in sensitivity and applicability. In this Bachelor thesis a new ^{222}Rn detector, the Cryo Monitor, is investigated on its sensitivity and applicability. The Cryo Monitor uses cryogenic pumping to drag ^{222}Rn particles close to a diode, registering alpha decays in order to increase its detection efficiency. This detector is quite robust and provides minimal detectable activities of as low as a few mBq.

Abstract

Im letzten Jahrhundert entwickelte sich unser Verständnis von den Gesetzten der Natur rasant. Dennoch blieben viele Rätsel noch ungelöst, wie zum Beispiel der Ursprung der Neutrino Masse, die Teilchen Natur Neutrinos und die Existenz von Dunkler Materie. Weltweit führende Experimente werden in ihrer Sensitivität von internen Hintergründen limitiert. Insbesondere das XENON1T Experiment das dunkler Materie in Form eines „weakly interacting massive particles“ (WIMPs) sucht, wird durch ^{222}Rn Emanation aus Detektormaterialien in seiner Funktion eingeschränkt. Eine sehr erfolgreiche Strategie um ^{222}Rn Emanation abzuschwächen ist die sorgfältige Auswahl oder Behandlung von Radon reinen Materialien welche zum Aufbau des Detektors verwendet werden. Daher gibt es große automatisierte Radon Prüfeinrichtungen welche den Radon Gehalt von Materialien untersuchen und aufzeichnen. Es existieren bereits viel unterschiedliche Detektormodelle um ^{222}Rn Emanation zumessen, welche sich jedoch in ihrer Sensitivität oder Anwendbarkeit stark unterscheiden. In dieser Bachelorarbeit wird ein neuer ^{222}Rn Detektor Modell, der Cryo Monitor, auf seine Anwendung und Sensitivität geprüft. Der Cryo Monitor benutzt das Prinzip des Cryogenischen Pumpens um ^{222}Rn Moleküle in die Nähe einer Diode zu ziehen, welche Alpha Zerfälle registriert, um so schließlich so seine Detektions Effizienz zu erhöhen. Dieser Detektor ist widerstandsfähig und in der Lage Aktivitäten bis zu einigen mBq zuverlässig zu detektieren.

Contents

1 Introduction

Observations on the Universe dynamics show a mass discrepancy that cannot be explained with gravitation as we currently know. This phenomenon is often explained with the existence of a non-luminous, massive component of the universe: *dark matter*. Dark matter is, up to date, known to only interact via gravitation with other matter of the universe.

The observations of the Planck satellite showed that the universe today consists of 27% dark matter and 68% dark energy. Only 5% of the matter is build up by the particles known from the standard model [1]. This leads to the necessity of a new particle beyond the standard model. A favored candidate for a dark matter particle is the Weakly Interacting Massive Particle (WIMP). WIMPs may have interactions with other standard matter particles but at strengths beyond previous and current experiments. Strong WIMP particle evidence beyond it's gravitational in-print is still not found. The WIMP model motivated numerous terrestrial and astronomical searches. One class of the terrestrial searches are the so called 'direct' searches, in which a recoil from a direct dark matter particle collision would be registered in an Earth based detector. Among them the experiments from the XENON series are deemed to provide the best chances of success.

Since WIMP events are very rare an extremely low background is required. In the XENON1T experiment, an upper limit on the WIMP-nucleon spin-independent elastic cross-section σ_{SI} was set to $4.1 \cdot 10^{-47}$ cm^2 for a mass of 30 GeV/c^2 [2]. During the development of each experimental stage backgrounds were constantly decreased. Henceforth the dominant source of background is produced by the constant emanation of ^{222}Rn from detector materials. This radioactive isotope ^{222}Rn is present in almost every material with natural origin. Its long lived mother nucleus ^{226}Ra is part of the primordial ^{238}U decay chain. To reduce this background, material used to build the detector are carefully selected. ^{222}Rn screening facilities are needed. There materials in different sizes and forms are screened down to sensitivities of few μBq. Currently the best ^{222}Rn detectors are sensitive to the alpha decay produced by ^{222}Rn, or subsequent ^{222}Rn daughters. There are several monitors available. These monitors vary in sensitivity, applicability and apply different techniques to maximise the efficiency of the detector. In this bachelor thesis, a new detector for monitoring ^{222}Rn in gas is developed. In contrast to other monitors this monitor increases its collection efficiency by freezing radon. This will be further explained in next sections.

In the following, the dark matter problem and its relation with low background experiments will be discussed in section 2. In section 3, I will give an overview over the radioactive isotope ^{222}Rn, its emanation and available detectors. The experimental setup of the here developed ^{222}Rn radon detector, the Cryo Monitor, will be illustrated in section 4. In section 5 I will describe in detail the commissioning this devise was undertaken after its first realisation was assembled. I will present a selection of data that has been taken, and quantify the performance of the devise in section 6. Finally in section 7, the most important results accomplished in this thesis are recapped and I will elaborate on future plans in order to improve the current setup and its applicability on future large-scale low-background experiments seeking for a WIMP particle.

2 Background in dark matter searches

Whenever dealing with a number of excess events that is almost compatible with zero, the sensitivity is entirely defined by the background uncertainties. Having large, or not fully under control, backgrounds impairs drastically the discovery power of an experiment. In the following lines, I will motivate two currently searched low-energy-signals, and the experiments and experimental-facilities behind it.

2.1 Fundamental physics quest

Most data from the dynamics of the Universe show a large imbalance between the gravitational forces exerted and the total mass generating these forces. To this problem I will refer as the *Dark Matter Problem*. The dark matter problem arised in 1933, Swiss astrophysicist Fritz Zwicky[3, 4] discovered that the Coma Cluster seemed to be achieving an impossible feat. He calculated an expected mass from the velocity distribution with the virial theorem and saw, that the galaxies are rotating with such speed that the gravity generated by their observable matter could not possibly hold them together. They should have torn themselves apart long ago. Zwicky explained this discrepancy between calculation and observation with an unseen mass he called *dunkle Materie* (dark matter). In 1980 Vera Rubin and Kent Ford further provided additional strong evidence[5] using galaxy rotation curves. They showed that most galaxies must contain six times more mass than the one observed. By the 1980s the existence of dark matter was widely recognised and is today considered to be one of the major unsolved problems of modern physics.

In spite of the overwhelming evidence for the existence of dark matter, it has not yet been observed directly. Its existence is only motivated from its gravitational interaction, and no other evidence has been found so far. From observations of galaxy clusters only rather vague conclusions can be drawn on the properties of dark matter particles. Apart from gravitational interactions, we do not see any measurable effects. It is more reasonable to exclude certain properties. Most obvious is that dark matter does not interact electromagnetically, hence it is invisible to electromagnetic observations. Moreover, the dark matter particle has no charge.
Observations show in interactions with ordinary matter the dark matter particle cannot excite or ionise. This excludes dark matter particles with high collisional energies. Properties of dark matter are constrained much further with modern experiments. Current limitations in interactions with other matter, leaves no particle in the standard model of particle physics that could make up dark matter. There are various hypotheses about what dark matter could consist of. One of the most promising candidates for a dark matter particle is the class of weakly interacting massive particles, known as WIMPs. The main characteristics of these particles are their large mass (GeV–TeV), and interaction only through the weak nuclear force and gravity, or possibly other interactions with cross-sections no higher than the weak scale [6]. Since they do not interact trough electromagnetic interaction, they are invisible for normal electromagnetic observations. Because of their large mass they would move at low velocities[7]. Since its proposal, the existence of such a particle has been constrained more and more, by better experiments. Still, current experimental limits do not cover the full parameter interaction-mass space in which this particle could exist.

There are other solutions for the dark matter problem aside from WIMPs. Not all hypotheses propose a new fundamental

particle and instead explain at least part of the missing matter with standard baryonic matter, such as protons or neutrons. For instance, the massive (astrophysical) compact halo object (MACHO), an astronomical body that emits little or no radiation, was believed for a long time to be a solution for the dark matter problem. However theoretical work showed that ancient MACHOs are not likely to account for the large amounts of dark matter now thought to be present in the universe[8]. An alternative explanation gives the *Modified Newtonian dynamics* (MOND) in terms of explaining why galaxies do not appear to obey the currently understood laws of physics. However this model cannot completely eliminate the need for dark matter in all astrophysical systems, since galaxy clusters show a residual mass discrepancy even when analysed using MOND[9]. In addition, MOND also fails to explain other observational evidence for dark matter as cosmic microwave background and structure formation.

Another yet not fully understood aspect of physics is the dominance of matter over antimatter in our Universe. The standard model of particle physics cannot explain this observation, hence there is need for extension of the model[10]. In most extensions of the Standard Model, neutrinos are assumed to be their own antiparticles. Particles that fulfil this requirement are called Majorana particles. These particles would imply the existence of neutrinoless double-β decay, which is an extremely rare lepton-number-violating radioactive decay process whose detection requires the utmost background suppression. So far a lepton number violation has not been unambiguously observed[11]. If indeed such a neutrinoless double-β decay would be observed it would motivate fundamental modifications of the Standard Model.

What these two physics quests have in common is the search of a very rare events. These events are in fact so rare that in spite of international efforts, neither a dark matter particle or a neutrinoless double-β decay have been observed so far. To increase their chances of success, experiments require extremely low backgrounds to reach sufficiently high sensitivities. That is where low-background techniques come into play.

Experiments in search of the dark matter particle can be divided in two classes: direct detection experiments and indirect detection experiments. Indirect detection experiments search for the products of self-annihilation or decay of dark matter particles in outer space. In contrast, direct detection experiments aim to detect dark matter particles by observing low-energy recoils of nuclei induced by interactions with dark matter particles passing through earth. An alternative to detecting dark matter particles in nature is to produce them in a laboratory, for instance at the Large Hadron Collider. In the following section I will introduce an example for a direct detection experiment in the search of dark matter, the XENON1T experiment.

2.2 XENON1T and the search of dark matter

Among the most promising class of direct detection experiments, searching for dark matter particles in the form of WIMPs, utilise liquid Xenon (LXe) as an efficient target for particle detection.

In the series of XENON direct dark matter search experiments, XENON1T has the strongest constraints on spin-independent cross-section. To shield the detector from cosmic ray events, the XENON experiments are located at the LNGS, at an average

depth of 3600 m water equivalent. The detector is a dual-phase time projection chamber (TPC) with a xenon gaseous GXe layer of xenon on top of the target. When a particle interacts with the LXe target energy is deposited, in the form of a scintillation signal (S1) and ionisation of electrons. The scintillation light is detected by two arrays of photomultiplier tubes (PMTs) on top and bottom of the detector. To collect the ionisation signal from free electrons, a drift field is applied. The electrons are extracted into GXe where they create a proportional second scintillation light signal (S2). From the time delay between S1 and S2 the location of the interaction is derived.

Particle physics experiments searching for rare events such as neutrino interactions, neutrinoless double-β decay and dark matter, have to fight against background of different origin: cosmic radiation, environmental background and intrinsic natural radioactivity of the experimental setup.

To minimise cosmic radiation, the XENON1T operates in one of the largest underground facilities, the *Laboratori Nazionali del Gran Sasso* (LNGS)[12]. Situated below Gran Sasso mountain in Italy, it offers the most advanced underground infrastructures in terms of dimensions, complexity and completeness. The 1400 metre-rock thickness above the laboratory represents a natural coverage that provides a cosmic ray flux reduction by one million times. Moreover, the flux of neutrons in the underground halls is about thousand times less than on the surface due to the very small amount of uranium and thorium of the Dolomite calcareous rock of the mountain.

For a further reduction of the background caused by cosmic radiation reaching the LNGS underground area and the intrinsic radiation from the rock, the TPC is located inside a water tank, instrumented with an array of PMTs sensitive to Cherenkov light emitted in water by muons. Last level of shielding is applied by fiducialization[1] inside the TPC volume, as the combination of S1 and S2 signals allow for a 3D reconstruction on the interaction place, acting the ultra-pure LXe as a self-shielding from the outside.
More discrimination is achieved by differentiating between events caused by nuclear recoils, *NR*, (WIMPs and/or neutrons) and electronic recoils, *ER*, (β and/or γ) and examining the ratio of S1/S2 further.

Throughout the generations of the XENON experiments external background sources were gradually decreased. Intrinsic background sources dominate currently. Prior to XENON1T, a large radon screening campaign took place to identify the most radon-clean materials to build the experiment. For XENON1T, the radioactive isotopes ^{85}Kr and ^{222}Rn make up most of the ER background. ^{85}Kr contamination appears mainly at the beginning, during the TPCs (and other parts) exposure to air. This means that once removed, krypton doesn't reappear. The ^{85}Kr concentration in LXe was reduced via cryogenic distillation to a sub-dominant level of ^{85}Kr/Xe = (0.66 ± 0.11) ppt, therefore contributes an ER background rate of 7.7 ± 1.3 events/(t·yr·keV)[2]. Instead, ^{222}Rn is constantly generated, and can therefore not be permanently removed. Thus, radon should either be prevented from emanating or the LXe has to be constantly purified from ^{222}Rn, which is very costly.
Fiducialization does not decrease the radon background. Due to the low chemical interactions and long lifetime of ^{222}Rn, radon atoms can decay everywhere in the TPC. Once radon is emanated, it distributes inside the LXe for $\sim$4 days and then produces an alpha that the PMTs see and can recognise as radon. However $\sim$ 20 minutes later ^{214}Pb (a ^{222}Rn daughter) decays

[1] Defining a region of interest at the central region of the TPC.

via β decay. This β signal looks like all other ER signals and is mixed with the rest of the backgrounds. In XENON1T, ^{222}Rn emanation contributes (71 ± 8) and (29 ± 4)events/(t·yr· keV)[2]. Other contributions to the ER background include γ emission from radioactive isotopes contained in the detector materials [13]. However these are contributions inferior compared to ^{222}Rn emanation.

In conclusion, a dark matter particle was not directly detected by the XENON1T but a upper limit on the WIMP-nucleon spin-independent elastic cross-section σ_{SI} was set to $4.1 \cdot 10^{-47}$ cm^2 for a mass of 30 GeV/c^2 [2]. XENON1T successor the XENONnT experiment, has a projected radon concentration of 1μBq kg, a factor lower than the achieved radon concentration in XENON1T[14]. The projected backgrounds can be seen inFigure 2.1. Unshaded areas correspond to the WIMP search energy for ERs and NRs, respectively. The largest ER background of ^{222}Rn is marked with an orange line. Bigger and better experiments after XENONnT require even lower radon concentrations. Therefore, the radon screening facilities need to improve.

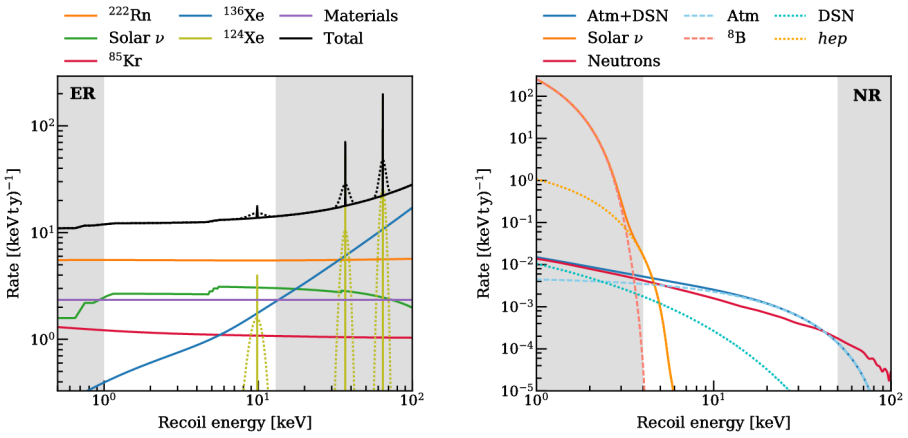

Figure 2.1: Projected energy spectra of the ER and NR backgrounds in XENONnT. Unshaded areas correspond to the WIMP search energy for ERs and NRs, respectively. **Left:** The largest ER background is due to the 1 Bq/kg activity concentration of ^{222}Rn (orange line). Additional backgrounds arise from solar neutrinos (green), double-β decay of ^{136}Xe (blue), ^{85}Kr (red). **Right:** The NR background contributions come from radiogenic neutrons (red) and CENS of solar neutrinos (orange)[14].

For completeness, XENON1T is also sensitive to other searches apart from WIMP. For instance, a small excess was observed in the electronic-recoil rate of XENON1T. The signature of the excess is similar to what might result from a tiny residual amount of tritium[2], but could also be a sign of something more exciting, such as the existence of a new particle known as the solar axion[3] or the indication of previously unknown properties of neutrinos [15].
Furthermore a neutrinoless double-β decay in a ^{124}Xe nuclei was direct observed by the XENON1T detector. This is presents a meaningful step in the search for neutrinoless double electron capture, the detection of which would establish the Majorana nature of the neutrino and would give access to the absolute neutrino mass[10]. This demonstrates that the low background and large target mass of xenon-based dark-matter detectors are well suited for measuring rare processes and highlights the broad

[2] A hydrogen atom with one proton and two neutrons
[3] A hypothetical elementary particle that is a possible component of dark matter

physics reach of larger next-generation experiments. However, other rare event searches of XENON1T, and the individual backgrounds they may suffer will not be discussed in this thesis.

3 The radioactive noble gas radon (^{222}Rn)

Radon is a colourless, odourless and tasteless noble gas, which makes it not detectable for human senses. At atmospheric pressure radon freezes at -71°C. It occurs naturally in the radioactive decay chains through which thorium and uranium slowly decay into lead and various other short-lived radioactive elements. Uranium is created during supernovae and neutron star mergers. Therefore its daughter ^{222}Rn is very common on Earth. It can be found in uranium ores, phosphate rock, igneous and metamorphic rocks such as granite, gneiss, and schist, and to a lesser degree, in common rocks such as limestone. This means that ^{222}Rn is present in everywhere in our daily life sometimes even in levels that are dangerous for humans.

All radon isotopes are hazardous owing to their radioactivity, gaseous nature, chemical inertness, and radioactivity of their decay products. The isotope ^{222}Rn is especially dangerous since its long half-life allows to diffuse trough soil, rocks and often building material. Even though radon cannot be spotted with human senses radon poses a real health threat as it is the single largest contributor to an individual's background radiation dose. Typical domestic exposures are of approximately 100 Bq/m^3. When radon decays, short lived daughter isotopes of polonium, bismuth and lead are created. Since radon and its decay products attach themselves to air molecules, they can be inhaled. Radon is almost completely exhaled, however its decay products accumulate in the lung and decay further thereby damaging the genome. The Bundesamt für Strahlenschutz (BfS)[16] estimates that 5% of all deaths linked to lung cancer are caused by the inhalation of radon. Since prolonged exposure to higher levels of concentration of radon increases the risk of lung cancer, the BfS advises to reduce the radon exposure in buildings by venting, sealing of doors and cabling to cellar and sealing entrance pathways to buildings.

As briefly mentioned in the previous section, radon can also be very dangerous for direct WIMP discovery machines, as XENON1T. Despite great efforts on selecting radon clean materials and manufacturing processes, radon was still the dominant background source for XENON1T. This section will focus on the isotope ^{222}Rn of radioactive noble gas radon, its emanation and detection.

3.1 Primordial origin of ^{222}Rn

There is no known stable isotope of radon. The ^{222}Rn isotope is the most stable with a half-life of 3.8235 days. It belongs to the ^{238}Ur and ^{226}Ra decay chain.
In the ^{222}Rn decay chain are four alpha decays. ^{222}Rn decays trough alpha emission first in ^{218}Po releasing a total of 5.5 MeV in the process. Right after follows the second alpha decay from ^{218}Po to ^{214}Pb with a half-life of 3.05 minutes and energy of 6 MeV. After a two β^- emissions the final for this Bachelor thesis relevant alpha decay occurs from ^{214}Po to ^{210}Pb. This decay has the shortest half-life of only 162 ms and a disintegration energy of 7.7 MeV [17]. Since ^{210}Pb has a half-life of 22 years, the last alpha decay is not relevant in the time scale of measurements that will be presented in the following chapters.

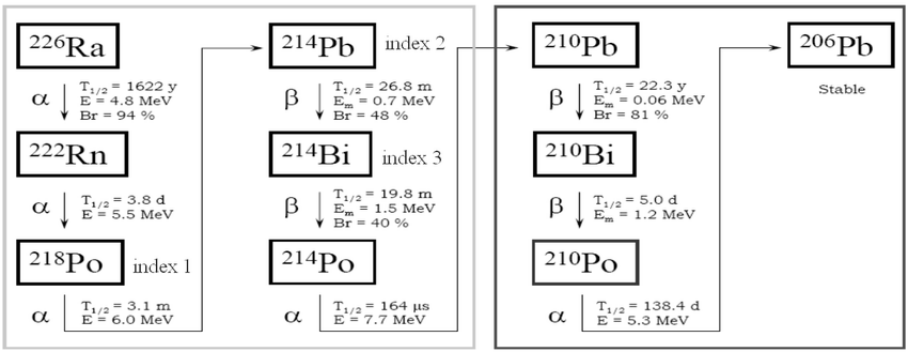

Figure 3.1: ^{226}Ra decay chain

3.2 ^{222}Rn emanation

Initially, ^{222}Rn is created in a material following the distribution of ^{226}Ra in it. After its creation, there are two ways for a radon particle to leave a material. The first process is emanation by recoil caused by an alpha decay. For this process the decay has to happen near the surface of the material. The second process is the diffusion of radon trough a material due to its noble gas properties [18].

3.2.1 Emanation due to recoil

When the mother isotope ^{226}Ra decays, the disintegration energy is to the greater part transferred to the alpha particle as kinetic energy since it is lighter than the daughter isotope ^{222}Rn. Due to conservation of momentum the radon atom receives a certain amount of momentum and energy. When the decay occurs directly on or below the materials surface, the recoil energy is sufficient to eject the radon atom from the material. The recoil energy E_{kin} can be written as following.

$$E_{kin} = Q_a \cdot \left(1 - \frac{M_{daughter}}{M_{mother}}\right) \tag{1}$$

With Q_a the disintegration energy and $M_{daughter}$ and M_{mother} the mass numbers of the mother and daughter isotope, respectively. The recoil energy in the case of ^{222}Rn is therefore 85 keV [19].

3.2.2 Emanation due to diffusion

The second process for the radon emanation is diffusion. Since radon is a noble gas, it rarely interacts chemically with its surroundings. Therefore the radon atom will not be fixed due to chemically bonds, as its mother nucleus ^{226}Ra, and diffuse easily in the material. If it reaches a boundary surface before its decay it will be emanated. There are multiple ways for diffusion. There is diffusion along grain boundaries, dislocation and atomic diffusion. [20]. However, radon diffusion is only understood qualitatively. Diffusion is expected to depend on other parameters as temperature, or material purity, but precision data is missing to support such relations properly.

Finally, different levels of emanation are expected from different materials, however, due to the limited effect of diffusion of dense materials, radon emanation is in the end very much related to surface impurities. Some manufacturing processes

(melting, cutting, storing, electropolishing, ...) alter the initial surface contamination of ^{226}Ra, therefore modifying the final radon emanation.

3.2.3 Simulation on radon emanation

In order to illustrate the concept of radon emanation, I developed a small toy Monte Carlo in the programming language python (more on toy Monte Carlos in [21]). The simulation assumes that 100% of the initial radon source is emanated, hence the simulated source activity is in the end the corresponding radon emanation from the source. A radium source at 2.06 Bq and a half-lifetime of 3.8235 days for ^{222}Rn[22] were given as starting parameters. The objective of this simulation is to obtain the time needed for radon to reach equilibrium activity, that is to say the equilibrium between particles that are created and decaying.

The simulation considers in each time loop how many radon particles are likely to be created/emanated. I also take into account the probability of a particle to decay during the same elapsed time (assuming 100% detection efficiency for pedagogical matters). Only radon decays and not radon atoms are shown by the simulation. Hence in Figure 3.2 the activity is given in Bq which is equivalent to number of radon decays per unit of time. This simulation should be sensitive to $\sim \mu$Bq, which is equivalent to 3.6 events per day. At these low statistics, the in-growth activity can be a dominant factor.
The time after equilibrium is reached is fully determined by the half-life of radon. After ∼13 days the source activity reaches 90%.

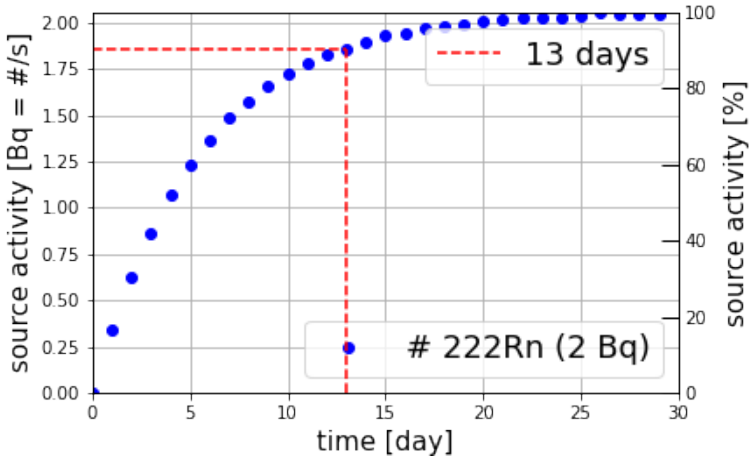

Figure 3.2: Simulation of the radon emanation. After ∼13 days 90% of the activity is reached (marked with a dashed red line). Full equilibrium is reached after ∼25 days of emanation.

This problem can also be solved analytically. The time dependent activity and the equilibrium activity are $A(t)$ and A_{eq}. $\lambda = \frac{ln(2)}{t_{1/2}}$ is the radioactive decay constant. For ^{222}Rn the half-lifetime is $t_{1/2} = 3.8235$ days

The derivative of the number of radon atoms $N(t)$ can be written as following:

$$\frac{dN(t)}{dt} = A_{eq} - \lambda N(t). \tag{2}$$

Integration leads to following equation with C as a international constant:

$$N(t) = \frac{1}{\lambda}(A_{eq} + C\lambda e^{-\lambda t} - A_{eq} e^{-\lambda t}). \tag{3}$$

Since no radon atoms existed at time zero $N(t) = 0$ and therefore the integration constant is $C = 0$

$$N(t = 0) = \frac{1}{\lambda}(A_{eq} + C\lambda - A_{eq}) = 0 \tag{4}$$

and finally the Equation 5 describes the number of radon atoms dependent on time:

$$N(t) = \frac{1}{\lambda} A_{eq}(1 - e^{-\lambda t}). \tag{5}$$

The above formula can be rewritten with $A(t) = \lambda N(t)$ as the activity:

$$A(t) = A_{eq}(1 - e^{-\lambda t}). \tag{6}$$

Further rearranging gives the time in dependence of activity:

$$t = \frac{ln(1 - \frac{A(t)}{A_{eq}})}{\lambda}. \tag{7}$$

Inserting an activity of of 90% of the 2.06 Bq in Equation 7, leaves us with an in-growth time of $\sim$12.7 days, so approximately 13 days. This agrees with the simulation's result.

As it can be seen measurements of radon sources near their highest activity require at least 13 days of emanation. This characteristic makes radon detection quite time consuming. To reach a desired activity every measurement requires some time for radon emanation.

3.3 ^{222}Rn- (or α-) detectors

Since ^{222}Rn emanation plays an important role in daily life, there are commercially radon detectors available. An example is the Lucas cell scintillation chamber. This detector is placed in homes or other buildings that are suspected to have high ^{222}Rn emanation. After weeks/days the user then sends the collector to a laboratory for analysis. Due to their use for detecting radon concentration that are health hazards, they are built to measure concentrations at levels of $\sim$100 Bq m^3. Hence Lucas cells are not capable at detecting ^{222}Rn at low levels, due to the high background from scintillator impurities.

As already mentioned in section 2, there are several experiments that are affected by the background caused by permanent decay of the radioactive noble gas radon. One solution to reduce radon background is to carefully select radon pure materials used to build the experiments. The difference between different radon instruments is how they maximise their efficiency at detecting the alpha emission from a radon decay. There are two problems all ^{222}Rn (or α) detectors have to fight. First problem is that radon will move everywhere before decaying, and not very likely in front of the alpha detection device (diode)

that is supposed to register the decays. Second problem is once decaying, the alpha can be emitted anywhere (isotropically). Generally, having small active volumes where radon is stored increases the efficiency but other techniques are applied to increase even further the sensitivity of alpha detector.

3.3.1 Miniaturised low-level proportional counter

The *low-level proportional counter* is considered to be the most precise method of radon monitoring. These detectors were originally built for the GALLEX/GNO experiment[23].

The detection principle is based on ionisation. A radon sample mixed with the counting gas is pushed into the active volume of ~ 1 cm^3 of the counter. There the gas is ionised by incoming particles. The free electrons are accelerated by an electric field towards the anode and cause further ionisation. Upon arrival, the electrons produce a current which is proportional to the initial ionisation.

Miniaturisation of the proportional counter helps to reduce background to $\sim$1 cpd (counts per day), because less material reduces internal background and the miniaturised counter is a smaller target for external background sources[24]. The effective counting efficiency measured in equilibrium between ^{222}Rn and its daughters for energies above 50 keV is $\sim$150%. In average out of three alphas, 1.5 are detected. Hence the detector can detect activities as low as 40μBq with 20% uncertainty.

3.3.2 Radon monitor - electrostatic chamber

Another approach for ^{222}Rn detection is the use of electrostatic chambers. These detectors collect the ^{222}Rn daughters on the active surface of a semiconductor diode. 88% of the time, ^{222}Rn daughters temporally form positive ^{218}Po ions which, in turn, are attracted towards the surface of the Si-PIN photodiode under the strong electric fields created within the vessel [25, 26]. The monitors that are employed at MPIK have 1 litre active volume and efficiencies of 30%. They have sensitivities of few mBq which is a factor 10 worse than proportional counters, however, there volumes are about a factor 1000 larger.

An advantage of radon monitors is that they are very robust, and can be operated at a large variety of temperature and pressures. This is especially convenient XENON1T, where xenon and radon are mixed together. Both being a noble gasses, it is very hard to separate them, and hence a radon sample from XENON1T cannot always be filled into a proportional counter[27]. These detectors were also used in the Super-Kamiokande neutrino experiment[28].

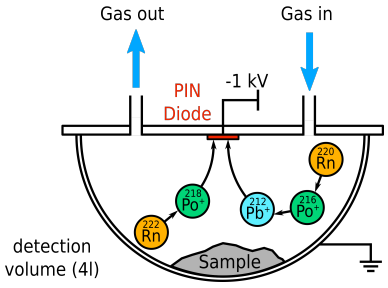

Figure 3.3: Schematic sketch of the Radon Monitor

3.3.3 Cryogenic radon monitor

The cryogenic radon monitor as introduced by M.Wojicik and G.Zuzel[28] is a rather new approach to detection of radon. The detector was originally designed for the ^{222}Rn concentration measurements in nitrogen, but can also be used for ^{222}Rn detection in air or emanation tests.
In contrast to the previous detectors the cryogenic radon monitor uses Cryogenic Pumping[29] to freeze radon from a carrier gas. Whenever a cold plate is brought into its cold state, radon particles contained into the main detector chamber are expected to sit/freeze on it. Like this, the collection efficiency from the subsequent alpha emission (into a ^{218}Po decay/transition) is maximised. The setup is as following.

Samples are let on radon tight vessels under emanation for few days, filled with a radon free carrier gas. Then, the emanated radon atoms can be brought into the detector chamber by transferring the gas from one volume to the other (expansion or pushing with extra carrier gas is used). This measuring chamber has a total active volume of 65 litres. To freeze radon, a double walled vacuum insulated container is placed above the chamber as can be seen in Figure 3.4 and is filled with liquid nitrogen (LN_2). Integrated in the container is a cold plate with a diameter of 40 mm and a thickness of 0.5 mm. On this cold plate radon should freeze and decay. A Ortec diode with a diameter of 50 mm is placed in front of the cold plate to detect any alphas. The diode is located to maximise its coverage from this cold-plate. Distance between cold plate and diode can be manually varied. All tests were carried out with a distance of 12 mm.

The prototype for the cryogenic radon monitor underwent multiple tests. First the background from the diode and cosmic ray events was determined to be A_{B0}=(0.93 ± 0.31) counts per day(cpd) and the second background components, caused by the permanent ^{222}Rn emanation inside the chamber, was measured to be A_B=24.5$\pm$ cpd. To obtain a maximum efficiency the authors tested both helium and nitrogen as a carrier gas at various pressures from $\sim$0 mbar to 400 mbar (210 mbar for nitrogen).

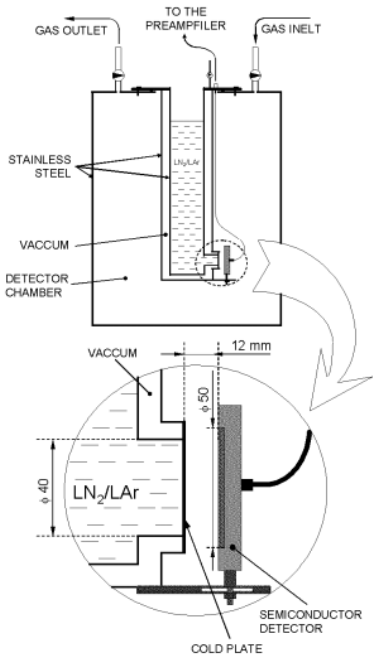

Figure 3.4: Design of the cryogenic radon detector by [30]

For the lowest pressure of both carrier gases (p$\sim$2 mbar) they found a maximum collection efficiency of (31.5$\pm$0.6)%. However, tests also showed a strong correlation between the collection efficiency, the carrier gas type and the pressure. Measurements with nitrogen as a carrier gas had lower efficiencies with increasing pressure and with longer collection time compared to measurements using helium. In general, higher pressures lead to longer collection times on the cold plate and an overall lower efficiency. The minimal detectable

activity (MDA) was calculated with the values for the measured background. It was determined to be 0.8 mBq (23 mBq/m^3).

The absolute efficiency can be written as $\varepsilon = \varepsilon_c \cdot \varepsilon_g \cdot \varepsilon_d$, where ε_c is the efficiency of radon collection on the cold plate, ε_g is the efficiency-based geometries and ε_d depends on the detection probability of the diode. For ε_g the claim an efficiency of 34% , based on the geometries of their cold plate, diode and distance between both. Considering that ε_c and ε_d are most definitely lower than 1, a maximum efficiency of (31.5$\pm$0.6)% seems to a quite successful achievement.

In the next section subsection 4.1, I will implement one realisation of a Cryo Monitor at Max Planck Institut für Kernphysik.

4 Cryo Monitor Setup

In this section, I develop a prototype of *Cryogenic Radon Monitor (Cryo Monitor)*. As described in previous sections (subsection 3.3), 'standard' radon monitors have active volumes of ∼litre scale and are instrumented with photo-diodes of a few square centimetre (∼cm^2). In order to obtain acceptable collection efficiencies (∼30%), standard radon monitors use negative electrostatic potentials to attract positively ionised radon daughters onto the diode surface.

The concept of Cryo Monitors, as introduced already in [30], use *Cryogenic Pumping* [29, 31] to achieve the same effect (e.g. drag the radon atoms close to the diode and improving the alpha collection efficiency at their decay). This detection technique allows direct detection of ^{222}Rn, unlike other radon detectors.

In this section I will introduce the technical details of the Cryo Monitor developed at MPIK. This setup was based on the idea developed by M. Wojcik and G. Zuzel [30] as described in subsubsection 3.3.3.

4.1 Conceptual design

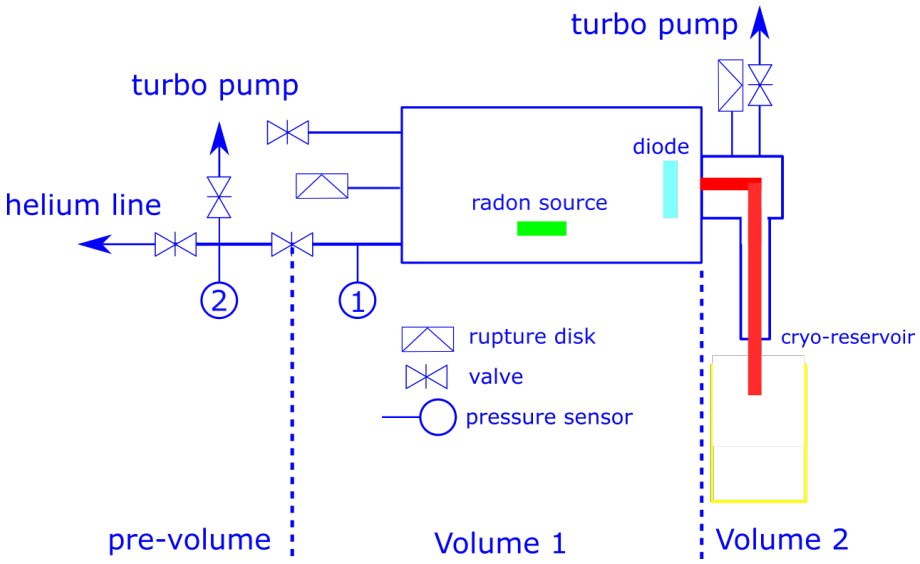

Figure 4.1: Sketch of the Cryo Monitor at MPIK. The detection chamber *Volume 1* is located in the centre. Volume 1 contains the diode and radon source. On the far right, the cold finger made from copper is on one end dipped in the *cryo reservoir* and on the other hand thermally connected with the cold plate. *Volume 2* is used to decrease loss of cooling power, by shielding the copper rod with a vacuum. On the far left the *pre-volume* is shown. This volume connects Volume 1 with a helium line and a turbo molecular pump.

Similar to the prototype detector[30] the Cryo Monitor has a main measuring chamber called *Volume 1* (V1). V1, where radon is expected to be enclosed, is defined by a circular volume limited by several valves. Integrated in the measuring chamber is a cold plate with a diode located directly in front of it. The diode is supposed to register the alpha decays of the frozen

^{222}Rn and daughters on the cold plate. Both instruments achieve cooling of the cold plate with LN_2.

Among the main differences is the location of the cryo reservoir that contains the LN_2. In the setup presented here the reservoir is not located on top but beside the detection chamber. The cooling power is transferred with a cold finger made from copper that is dipped into the LN_2. The copper rod is vacuum isolated and guided through a flange into the main measuring chamber. The temperature of the cold plate is vital for a proper working monitor as will be further illustrated in subsection 4.5. The end of the cold finger functions as the cold plate. Directly connected to V1 is a rupture disk, a pressure sensor and two valves. V1 is filled with gas or evacuated through the *pre-volume* directly connected (labelled as 'pre-volume' shown in the left part of Volume 1 in Figure 4.1). The isolation volume around the cold finger is called *Volume 2* (V2, shown in the left part of Volume 1 in Figure 4.1). The vacuum insulation V2 is meant to improve thermal conductivity of the rod, by avoiding thermal losses through radiation so that they are subdominant in comparison to IR-radiation losses. In order to improve the thermal insulation of V2, the volume evacuated down to $< 10^{-6}$mbar. A rupture disk was also installed in V2, to prevent the hazard created by having oxygen, or other gases, being liquefied inside V2 while the cold finger is tipped in liquid nitrogen. When the gases return to their gas states at room temperature, they could expand and create dangerous over-pressure.

4.2 Technical design

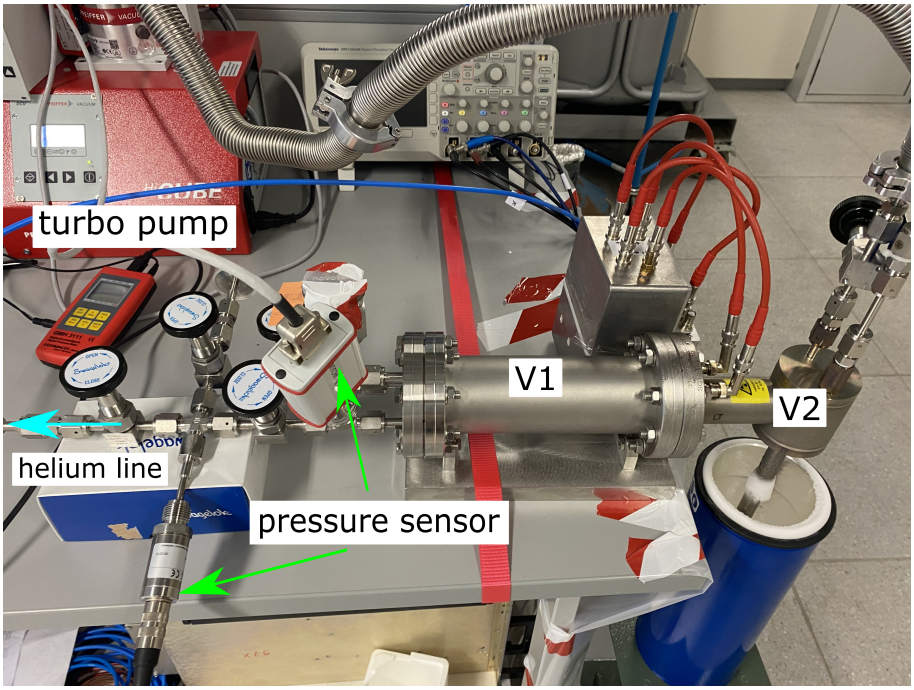

Figure 4.2: Picture of the Cryo Monitor. Near the centre of the picture is the cylinder volume of the detector chamber (V1). On the right the cold finger tipped in the dewar filled with liquid nitrogen is shown partially insulated by V2. At the left, the pre-volume assists with gas and pump connections.

The main volume chamber V1 is composed of a not electropolished stainless steel pipe of $\sim$ 21.6 cm length, inner diameter of $\sim$ 9.2 cm giving a total active volume of $\sim$ 1.434 l.

The Diode is fixed in a holder made from Polyetheretherketon (PEEK) directly aligned on the same axis as the cold plate to maximise the alpha detection efficiency. The distance to the cold plate is $\sim$ 2.5mm.

The cold finger made from copper has a diameter of $\sim$ 10 mm and is $\sim$ 47.5 cm long. It is bend in the shape of an 'L' as can be seen in figure A.1. The cold-fingers diameter is reduced to half when entering the flange between Volume 1 and Volume 2. Since the end of the copper rod is the cold plate, its diameter is $\sim$ 5mm. To minimise any heat loss, the copper rod is lead through the vacuum-insulated chamber Volume 2.

Several commercially available components and/or instrumentation were used in the process to assemble and commission the Cryo Monitor. In the following I will give a brief introduction to them.

4.2.1 Pressure sensors

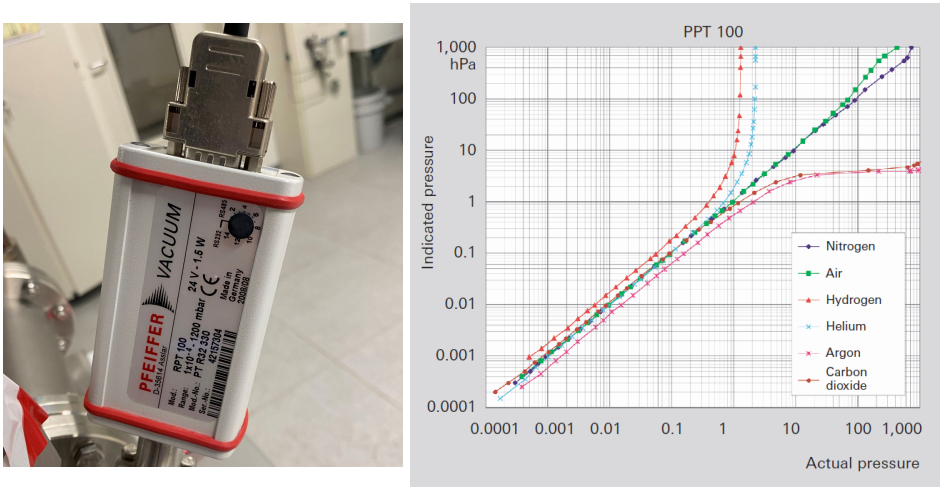

Figure 4.3: **Left:** RPT 100 **Right:** Pressure dependence of the Pirani vacuum gauge on gas-types. It is apparent that after reaching 1 mbar the indicated pressure for helium is higher than the actual pressure.

There are many different pressure sensors available. They differ in range, sensitivity and dependence on the gas type. After research and testing different models, I chose a combination sensor to cover both high-pressure and vacuum ranges.
In particular I used `Piezo/Pirani combination RPT 100 gauge` from Pfeiffer Vacuum[32] , with an absolute range of 10^{-4} – 1200 mbar and a sensitivity of $\pm 0,5\%$ (at 5 – 1200 mbar) to monitor the pressure of (V1).
It is important to notice that for lower scales the pressure is measured by the Pirani sensor, which is gas dependent (Figure 4.3 shows the indicated pressure in dependence of the gas type). Reaching 1 mbar of helium or more the sensor indicates higher pressures than the actual pressure.
To crosscheck and in order to extend the pressure range into the low-vacuum regime, I also used the model `MSD 2,5 BAE` from Greisinger[33], with an absolute range of 0-2500 mbar and a resolution of 1 mbar. This second pressure sensor is connected to the pre-volume only, and hence a cross-calibration between both sensors can be done with the valve in between opened.
The pumping station unit used in this setup (see subsubsection 4.2.5) was also equipped with a pressure sensor readout, a `PKR`

251 a Pirani/Cold cathode ionization vacuum gauge. It has a pressure range of $5 \cdot 10^{-9}$~10^{-3} mbar with a precision of $\pm 30\%$ (datasheet from pfeiffer[34]).
The RPT 100 is labelled 1 and the Greisinger is labelled 2 in Figure 4.1.

4.2.2 Temperature sensor

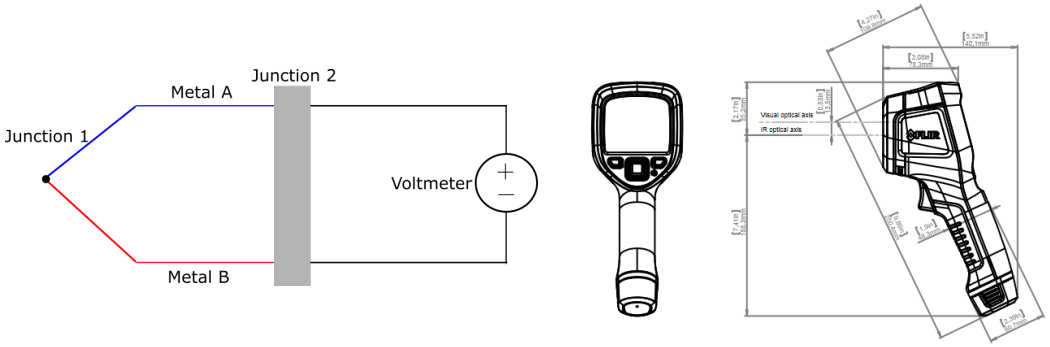

Figure 4.4: **Left** Schematic design of a thermocouple sensor **Right** Design of the infrared camera

In the experiment a constant temperature monitoring of the system was not needed and temperature sensors where only temporary used to evaluate the performance of the cold finger. Main differences in temperature sensor instrumentation arise whether their applicability is meant to be on gas, liquid or solid.
In temperature tests (see subsection 5.2) a thermocouple temperature sensor was used. A thermocouple sensor consists of two wires of different metals that are connected at two points, as can be seen on the left in Figure 4.4. When both junctions are at different temperatures an electromotive force (e.m.f.) is induced in this closed circuit. The amount of induced voltage is proportional to the temperature difference.
The advantage of this type of sensor is that it operates across a wide temperature range, approx. from -200 °C to 1750 °C and can be used to measure the temperature at one particular point in a setup. However, it is known for low accuracy.
To confirm the results and to get further insight in the heat-transfer in the Cryo-Monitor structure I also used an infrared camera of the model E6 from the FLIR[35]. The infrared camera is reliable up to -20°C and thus used only for a qualitative overview.

4.2.3 Valves

Valves are typically used to easily connect and disconnect volumes. Main characteristics of a valve are how much pressure it can sustain, the quantity of flow regulation and how good is it at keeping a vacuum (typically referred as pressure resistance, adjustability and tightness). Five Stainless Steel Bellows Sealed Valves in the size of quarter inches with a gasket body-to-bellows seal from Swagelok[36] are used. They were chosen for following arguments: they are resistant to pressures up to 100 bars, flows in our setup do not need to be adjusted (however Swagelog valves are typically installed through VCR fittings), they are widely available in vacuum related installations and they are specifically defined to sustain leak rates down to $\sim 4 \cdot 10^{-9}$ mbar·l/s. Even though these valves present many advantages, they are very sensible to be miss-operated and their tightness can largely degrade over time. This applies to all our valves in Figure 4.1.

4.2.4 Fittings & Feed-through

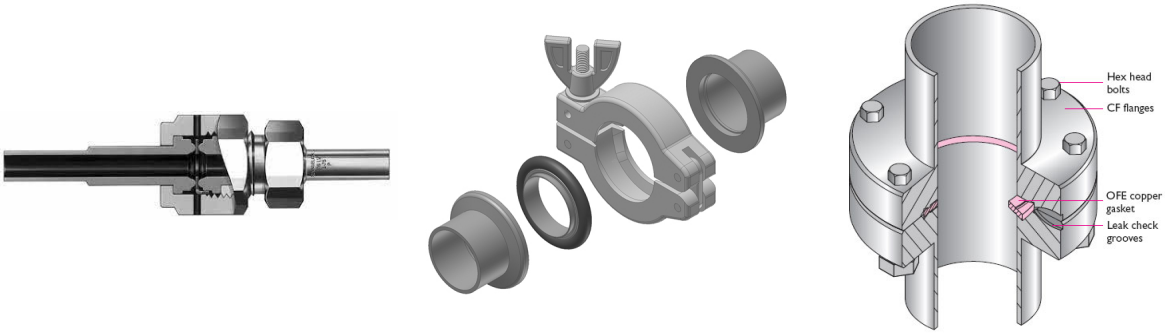

Figure 4.5: Schematic drawing of VCR, KF and CF fittings (left, center and middle, respectively).

Fittings are typically used to construct volume and pipe shapes starting from smaller components (easier to build and commercialise on large scale). Different commercial fittings are available, again similarly to valves, they mainly differ on their high-pressure resistance, vacuum exposure tightness and easiness to mount. It is common for all fittings to use an in-between gasket, placed between the two components to be fixed together. Such gaskets are either for single use only or can be reused multiple times. They are meant to seal the connection tight and to avoid damaging the two surfaces that will be put in contact in order to prevent future air-leaks.

KF To connect the volumes to the pumps a standard quick release flange known by the name Klein Flansch (KF) is used. They are typically only resistant up to 1 bar but are very good at keeping vacuums down to $\cdot 10^{-9}$ mbar. In the case of the Cryo Monitor the gaskets are used multiple times.

CF In Volume 1 two CF-DN-63 Flanges are used. These flanges are made from stainless steel and use a copper gasket to achieve vacuum conditions. They are among the most common option for cylindrical symmetric volumes that are larger than a litre. The copper gasket is used only a single time.

VCR Metal to metal parts were connected by the use of quarter inch VCR fittings. The seal on a VCR assembly is achieved by the compression of two beads during the engagement of a male nut and a female nut as can be seen in Figure 4.5. They are certified on high pressure ranges up to hundreds of bars (only for small diameters of few inches). A one use soft-metal gasket is used. Adjusting them is rather easy (only need a couple of keys), and once being fixed, they are quite resistant to impacts, vibrations and deformations. In the setup in Figure 4.1 $\sim$16 quarter inch VCR fittings were used.

Rupture disk Two rupture disks were installed. In V1 the rupture disk was tarted at $\sim$2.7 bar and the rupture disk in V2 at $\sim$16 bar. To connect them to the setup all rupture disks have VCR adaptors. The location of both rupture disks can be seen in Figure 4.1.

4.2.5 Turbo molecular pump (TMP) and leak-tester

A turbo molecular pump, model `HiPace 80`, was used to evacuate the different volumes of the system. The pump module is a Hybrid Bearing pump, that allows to pump at a pumping speed of 67 $l \cdot s^{-1}$ for N_2 (data sheet from pfeiffer[37])
The final pressure without gas ballast is $\sim 5 \cdot 10^{-10}$ mbar.
A Pirani/cold cathode ionization vacuum gauge was installed in front of the turbo module to read the pressure (as described in subsubsection 4.2.1).

Another important equipment when discussing leak-tight constructions are leak-detectors. Leak detectors are basically composed by two pumps (a primary and a turbo) and a measuring chamber. The gas reaching the measuring chamber is ionised and deflected through a magnet in order to select specific mass-to-charge ions. Helium ions are typically used to verify the tightness of the system down to 10^{-12} mbar·l/s. After any hardware modification, the tightness of the system was verified using a commercially available leak-detector, model `ASM 340`.

4.3 Alpha sources

The main objective of our Cryogenic Monitor setup is to be sensitive to alpha emission. In order to characterise the setup, two low-activity (<10 Bq) alpha sources were used.

4.3.1 ^{241}Americium source

A ∼10 Bq ^{241}Am source was used to characterise the first response of the diode. ^{241}Am isotope decays to ^{234}Np releasing an alpha particle with an energy of 5,486 MeV. The Americium isotope is contained within a circular (d≈ 1cm^2) surface that was located directly in front of the diode as can be seen in Figure 4.6.

4.3.2 ^{222}Radon source

A ^{222}Rn source was used, based on solid 226-Radium implanted onto an SS disk (d∼1 cm). This sample was produced at the ISOLDE facility at CERN, by accelerating and implanting ions through collision onto it [38]. From here after, this source will be called the Isolde source, or simply Isolde.

After the implantation, two independent measurements from the ^{226}Ra activity from Isolde were taken, with alpha and gamma spectrometry, that showed an activity of about ∼9 mBq (both measurements performed in-house at MPIK, more details at [39] and [38]). Both measurements are in agreement with the expectations from the ISOLDE implantation process.

Finally, a third measurement was performed to estimate the radon ^{222}Rn from the Isolde source. This measurement was also performed in-house [23], with the result of (2.07±0.05)Bq. Note that this is the only measurement that will be relevant for this bachelor thesis, as the Cryo Monitor will only be sensitive to the alphas from the emanated ^{222}Rn.

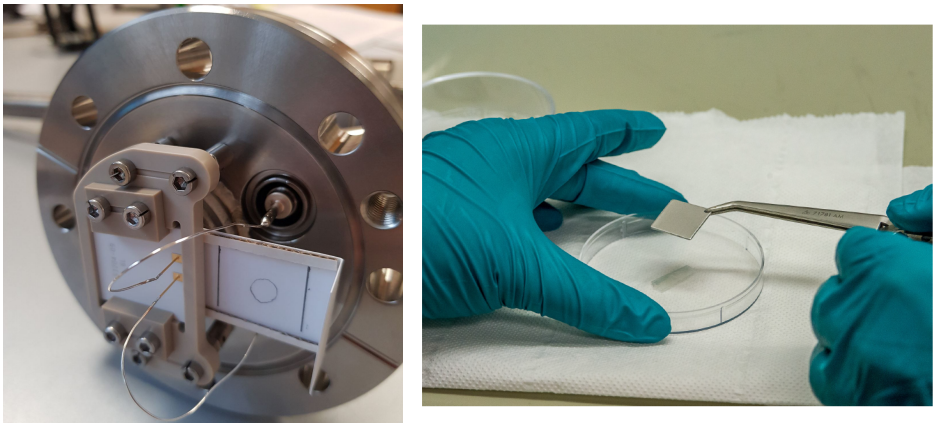

Figure 4.6: **Left** ^{241}Am source: An Americium alpha source is located directly in front of the diode through an easy slide-in-window. The circular region is enclosing the deposited Americium source. **Right** ^{222}Rn source: Isolde

4.4 Diode, Electronics & DAQ

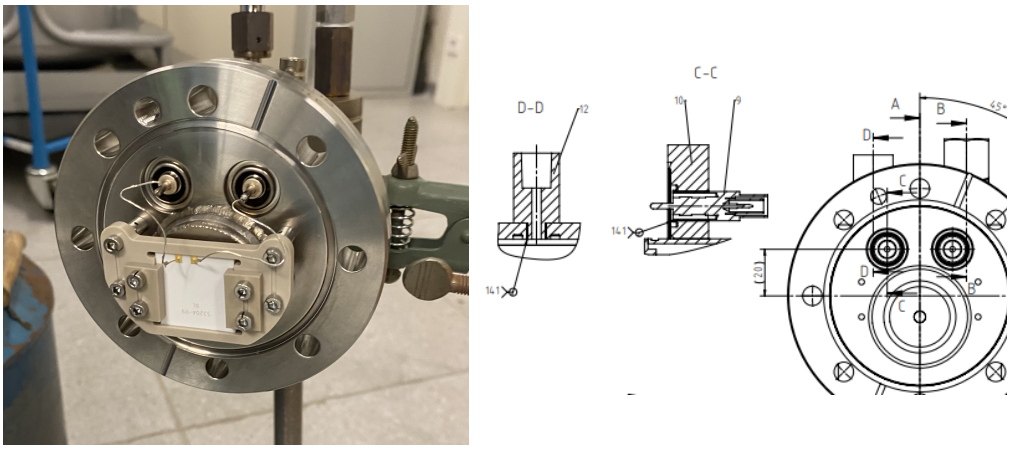

Figure 4.7: **Left:** Diode in holding made from PEEK. **Right:** Technical drawing of the BNC feed-trough.

4.4.1 Diode

In the Cryo Monitor setup a silicon pin diode is used. The working principle is quite similar to a p-n diode.
The p-n diode consists of two semiconductor layers. One layer is of p-type (contains an excess of holes[4]) and the other layer is of n-type (contains an excess of electrons).When the layers are combined a momentary flow of electrons occurs from the n to the p side resulting in a third region between the two where no charge carriers are present, the depletion region. The diode is designed to be operated in reverse bias[40]. A negative voltage is applied on the p-side and a positive to the n-side, thereby widening the depletion region.
When an alpha of sufficient energy strikes the diode, it creates an electron–hole pair. If the absorption occurs in or near the junction's depletion region the electric field moves holes toward the anode, and electrons toward the cathode. Thus, a photocurrent is produced. The produced current is proportional to the energy of the passing alphas.

What distinguishes the PIN diode from a p-n diode is that between the p and n layer there is an undoped intrinsic semiconductor. This approach has the advantage that it is better suitable for high voltages.

We used the photodiode model `S3204-08` from Hamamatsu[41]. It has a photosensitive area of 18 × 18 mm (see data sheet[42]). Anode and cathode were kept at different potentials, with a difference of 8 Volts between them (bias voltage, as in standard radon monitors).

4.4.2 Electronics

Cathode and anode signal are extracted from the main chamber of the monitor through dedicated feed-through ports, as seen in Figure 4.7, from where they are wired into the preamplifier. This wire is very well isolated and has a short length of ~ 5 cm to minimise catching additional electrical noise.

[4]Lack of an electron at a position where one could exist in an atom or atomic lattice

Charge sensitive preamplifier (CSP) To amplify the diode signal-amplitude we use a charge sensitive preamplifier also known as (CSP) made in *in-house*. Their design offers low noise, stability, and their integrating nature provides an output proportional to the total charge flowing from the detector during the pulse event. Both CSPs are powered with a 5 Volt power supply.

Differential amplifier A further noise reduction is achieved by a differential amplifier. First the cathode and anode signals are checked whether they sum up to zero. If this is the case both signals are fed into the differential amplifier, where they are subtracted and their difference is amplified by a factor 50.

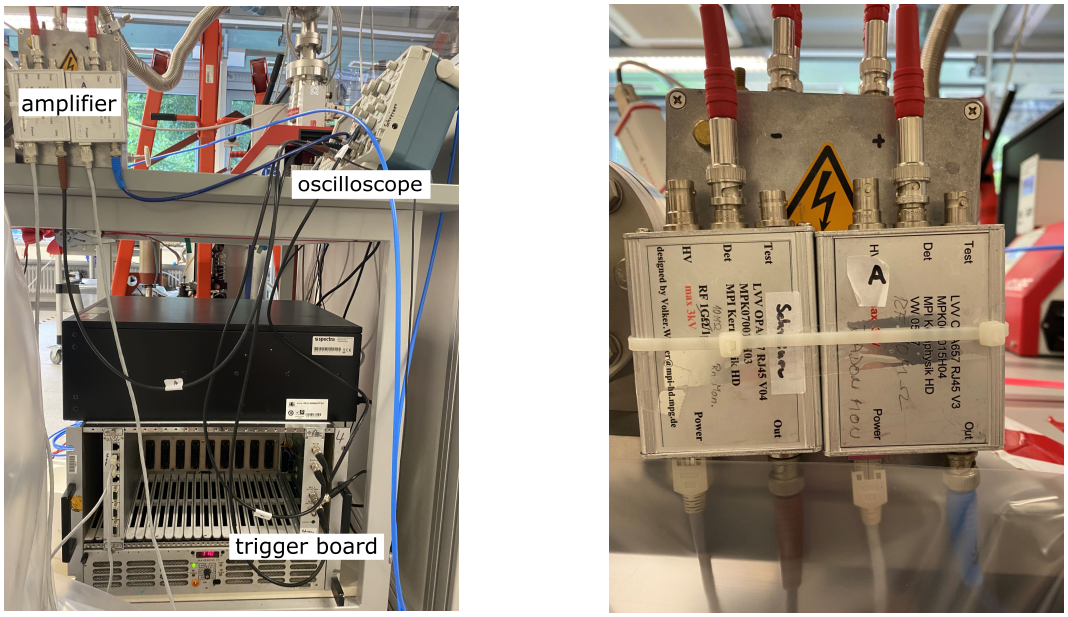

Figure 4.8: **Left:** Electronic setup. Labeled are the preamplifier, the differential amplifier and a oscilloscope **Right:** Charge sensitive preamplifier made in-house

4.4.3 DAQ

The signal is finally fed into the Multi Channel Analyser of the model `MCA-3A` from FAST ComTec [43] (see data sheet[44]). First the base line of the signal is determined. The difference in voltage between base line and signal is assigned into a channel. A low energy threshold of 350 mV is applied to further reduce any noise. I verified that the noise rate with this threshold condition is less than 1 Hz, hence dead-time of the system is negligible and can be safely ignored. The produced histogram was summed up every 60 seconds and saved with unique time stamps for all events recorded within the previous run.

4.5 Cold finger thermodynamic properties - COMSOL

As described in subsection 4.1 the cooling power of the cold finger, and the subsequent radon freezing efficiency, is crucial for a successful detection of radon.
The minimum requirement of the system is that the copper surface embedded inside the main chamber of the monitor reaches temperatures below -71°C, the freezing temperature of radon (as already explained in section 3). To understand the thermal properties of different setups a commercial software was used to simulate the thermal properties of the cold-finger. We used COMSOL[45] for this purpose.

The simulation uses a 2D model of the cold finger to plot the temporal change of the temperature of the Cryo Monitor. The in subsection 4.2 lengths and widths of the cold finger given were used for the 2D model. Different however to the actual setup is that instead of the round 'L' shape we used a 90° angle for the kink of the cold finger (as can be seen on the left of Figure 4.10). The isolation vacuum also differs from the real Volume 2. To simplify the model Volume 2 was changed to a pipe surrounding the copper rod.
Two thermal processes can take place in the simulation: material-to-material heat-transfer and surface-to-surface radiation. For copper and stainless steel, we used a heat capacities of 385[J/(kg·K)] and 475[J/(kg·K)]. The initial temperature of the entire setup is 20°C. When the simulation starts, the edges of the cold finger length, not surrounded by the isolation vacuum, are set to be at constant liquid nitrogen temperature (-196°C).

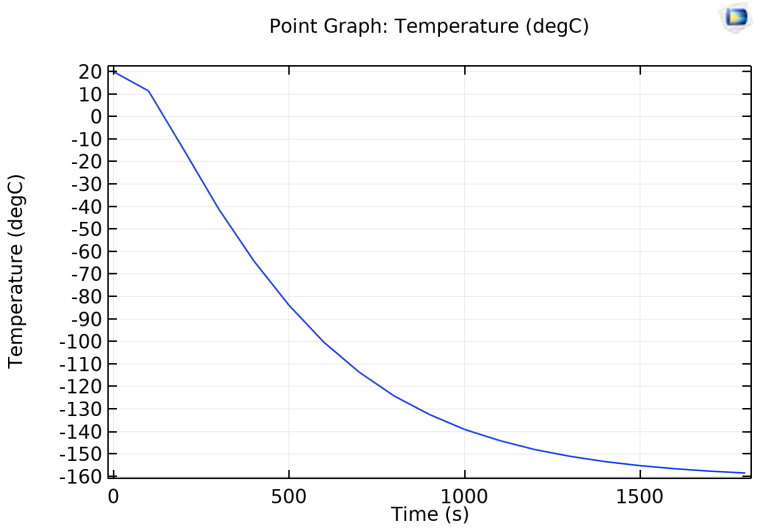

Figure 4.9: Temperature evolution at the centre of the cold plate. After 8 minutes the freezing temperature of radon is reached. After 30 minutes the temperature converges and a lowest temperature of $\sim$ -160°C is reached.

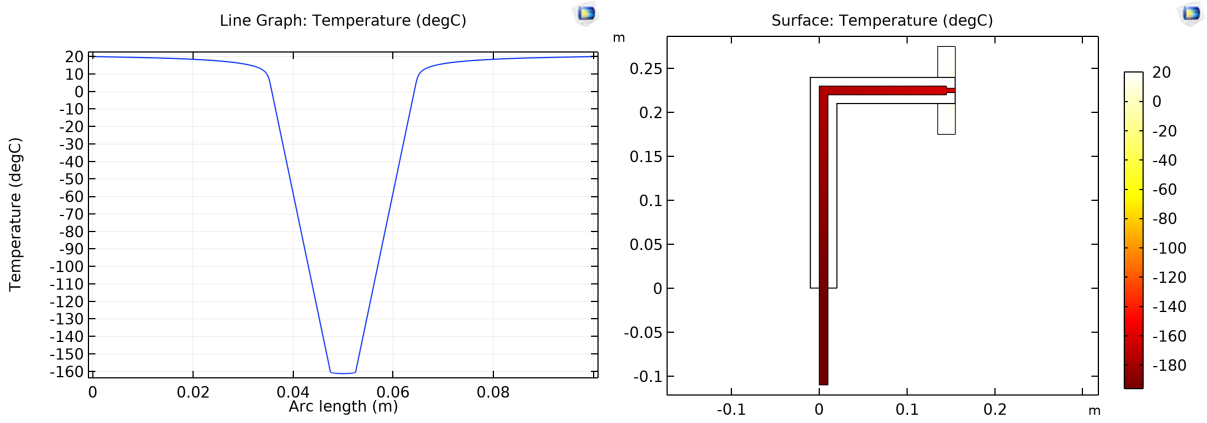

Figure 4.10: **Left:** Temperature distribution over cold plate. At the centre where the cold plate is located the lowest temperature of -160°C is reached. At the stainless steel edges the temperature increases rapidly. **Right:** Equilibrium temperature distribution of cold finger and 2D cold finger simulation. As expected the end of the copper rod is at liquid nitrogen temperature, while the cold plate is slightly warmer

Figure 4.9 displays the temporal temperature evolution of the cold plate. The minimal temperature of $\sim$-160°C is reached after approximately half an hour. Far sooner after just 8 minutes the freezing temperature of radon is attained.
In Figure 4.10 we see temperatures after thermal equilibrium. On the left the temperature distribution on the cold plate and the stainless steel surroundings is shown. Outside the edges of the cold plate the temperature rises rather quickly.
The right figure features the final temperature of the entire cold finger. As can be expected the the temperature of the rod declines towards the nitrogen tank.

5 Cryo Monitor commissioning

In this section the commissioning of the Cryo Monitor is described. Even though the theory behind the Cryo Monitor is fairly simple, several problems occurred at first. To understand and solve these problems the monitor was tested on tightness, temperature, electronics and correct data acquisition. With the knowledge gained from the measurement of this chapter several improvements were achieved to ensure the experimental success.

5.1 Tightness of the system

For any system that works in vacuum, tightness is crucial. From setups prior to the Cryo Monitor presented here it was known, that incoming water vapour can freeze on the cold plate and subsequently prevent radon to be trapped effectively. For detector Volume 1 primary concern is incoming water vapour, freezing on the cold plate that would subsequently prevent radon to be trapped. In the isolation vacuum V2 leak would increase the heat transfer of the surrounding to the rod of the cold finger, ultimately impairing the cooling of the cold plate.
At the beginning pressure increases were observed in both volumes. To locate the source of incoming gas I checked for leaks and outgassing.

5.1.1 Leak test

To detect leaks helium was used as a test gas and the leak detector model described in subsubsection 4.2.5. To increase the helium concentration, I sprayed helium at spots of the setup where leaks were suspected.
This was done after every hardware intervention and no leaks over $2 \cdot 10^{-9}$ mbar·l/s were found. The leak rate is calculated as below:

$$r_{leak,i} = \frac{\Delta p \cdot V_i}{\Delta t}, i \in 1,2 \tag{8}$$

With Δp as the pressure increase in Δt amount of time. V_i is the corresponding volume.

5.1.2 Outgassing

Outgassing is a major issue in creating and maintaining clean high-vacuum environments. Materials normally not considered absorbent can release enough light-weight molecules to interfere with industrial or scientific vacuum processes. This effect is especially strong when using a non-metallic material such as a polymer, adhesive, rubber, or potting compound/ epoxy.
Usually outgassing occurs in two ways. Either molecules are diffusing through the bulk material of a vacuum chamber, entering the surface and desorbing from it. Alternatively, molecules which have been adsorbed previously, usually during venting of the vacuum chamber, desorb again, when the chamber is pumped to vacuum. Both effects have the same consequences: They limit the lowest achievable pressure in a vacuum chamber and bring impurities into the vacuum system. The latter problem is especially inconvenient for instruments in spacecrafts because, outgassing products can condense onto optical elements, thermal radiators, or solar cells [46].

For the Cryo Monitors case outgassing products can strongly impair the devices performance. If their freezing point is below ∼-160°C like it is the case for carbon oxide, gas might freeze on the cold plate and potentially act as an insulation layer preventing radon to freeze onto the surface. Since air is composed of 0.0407 % CO_2 and water is also known to be absorbed, our efficiency will decrease in a system with large outgassing rates.

There are several techniques to reduce outgassing as much as possible in a vacuum tight system. Firstly, it is advisable to use materials with a very low outgassing rate. However sometimes it is unavoidable to use materials with higher rates like in this case the holding of the diode made from PEEK.

Since diffusion is a temperature dependent process, outgassing will be much faster while heating. Therefore, baking the setup at higher temperatures while pumping will decrease outgassing rates.

In the setup it was important not to exceed 80°C while baking since the diode would otherwise be damaged.

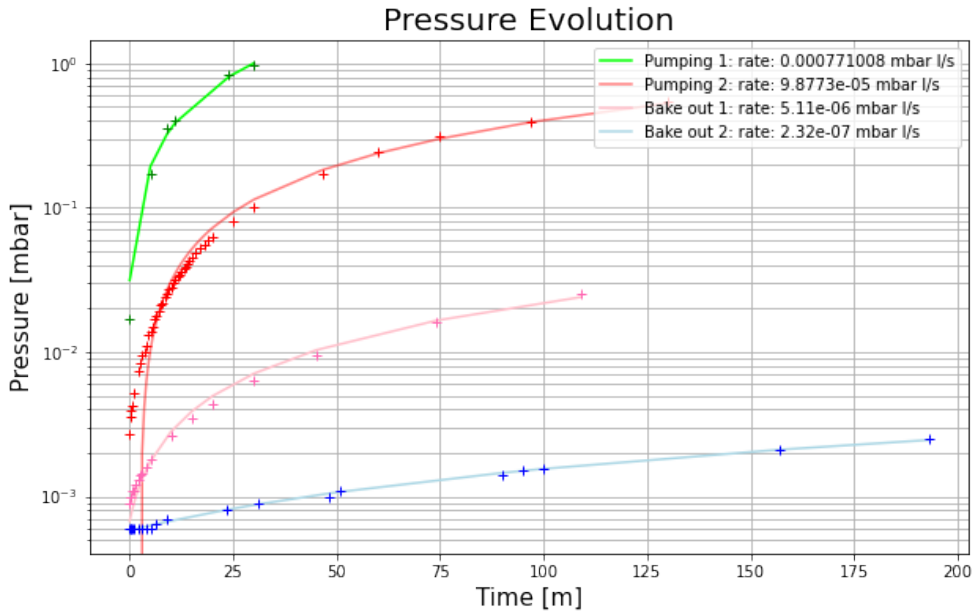

Figure 5.1: The pressure rate increase after each outgassing phase in Volume 1. There is a significant decrease after each pumping and/or baking campaign. The overall trend of data seems to point towards an internal source of gas, more than an external leak. Measurements in section 6 were taken after Bake out 2, where outgassing rate is 2.32 $\cdot 10^{-7}$mbar·l/s.

To confirm that the pressure increase was indeed caused by outgassing multiple tests were performed. In these tests the Cryo Monitor was pumped while baking at 65°C or alternatively without baking. After each outgassing phase the pressure of the closed Volume 1 was monitored and the pressure increase rates compared.

Pumping V1 for a day already decreased the rise in pressure by a factor 10 (difference between Pumping 1 and 2 in Figure 5.1). Baking turned out to be also very efficient at speeding up the outgassing process, as can be seen from lines Bake out 1 and 2 in the same figure. The lowest outgassing rate achieved was of $2.32 \cdot 10^{-7}$ mbar· l/s, fitting Equation 9. To each outgassing process a line model was fitted. The slope is therefore the outgassing rate divided by the volume V1. The model used for fitting is as follows:

$$p(t) = t \cdot \frac{r_{outgassing}}{V_1} + p_{min} \tag{9}$$

With $r_{outgassing}$ as the outgassing rate in mbar·l/s, t as time and p_{min} as the minimal pressure (reached by extrapolating the fit). In Figure 5.1 it is shown how the outgassing rate becomes smaller after each test. However, the measurements are still linear distributed which either indicates that the outgassing has not yet reached its saturation or the increase in pressure is caused by a leak. Latter is unlikely since the outgassing/leak rate decreased after each pumping and heating campaign. This hints to an internal source of gas, and rules out an external leak that would have kept a constant leak rate. Furthermore not a leak even close to the magnitude of 10^{-7} mbar·l/s was observed while leak testing(see section subsubsection 5.1.1).

5.1.3 Leak-test under cold mechanical stress

To confirm that a leak is not created while cooling the Cryo Monitor or in the warming up phase, the pressure was monitored before, during and after cooling. The pressure evolution is plotted in Figure 5.2. The measurement started on Day-0 at 18:00 (most bottom line). On Day-1, at about 12:00 the cold-finger was immersed in LN2, until 17:00. Data taking continued until 8:00 of Day-4. The x-axis runs from 00:00:00 to 23:59:59 where data from all days is overplotted. As can be seen the cold test did not significantly alter the pressure evolution.

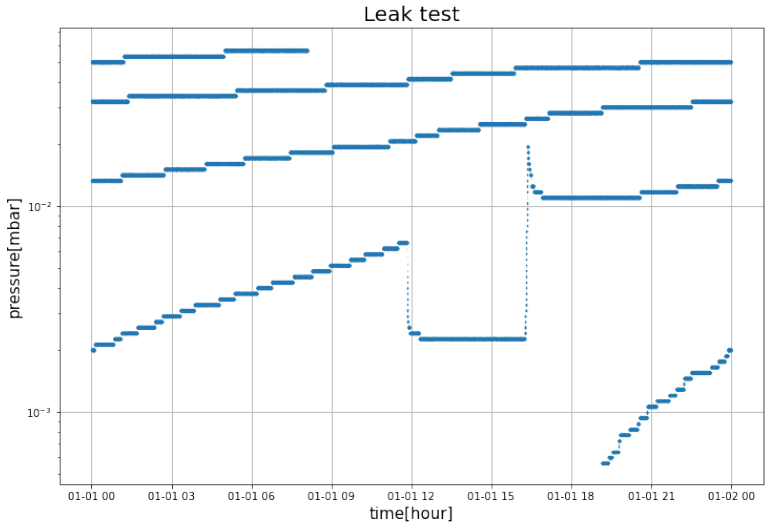

Figure 5.2: Pressure evolution after, during and before cooling the Cryo Monitor. Measurement started on Day-0 at 18:00 (most bottom line). On Day-1, at about 12:00 the cold-finger was immersed in LN2, until 17:00. Data taking continued until 8:00 of Day-4. X-axis runs from 00:00:00 to 23:59:59 where data from all days is overplot.

5.2 Temperature of the cold plate

The temperature of the cold plate was measured with the thermocouple sensor described in subsubsection 4.2.2.
Since the wire was too long for the cold plate, it was curled up into a spiral close to the cold plates size. The flange connected to the cold finger was separated from the setup and the temperature sensor placed onto the cold plate. To improve the thermal conductivity the second and third measurement were performed with a copper plate placed on the sensor as can be seen in Figure 5.3.

The tests were done without pumping and alternatively while pumping Volume 2. As can be seen in Figure 5.4 the freezing temperature of radon is achieved after cooling the cold finger while pumping for about 6 minutes and the final temperature is 20°C lower. Because of these observations, Volume 2 was pumped while taking measurements.

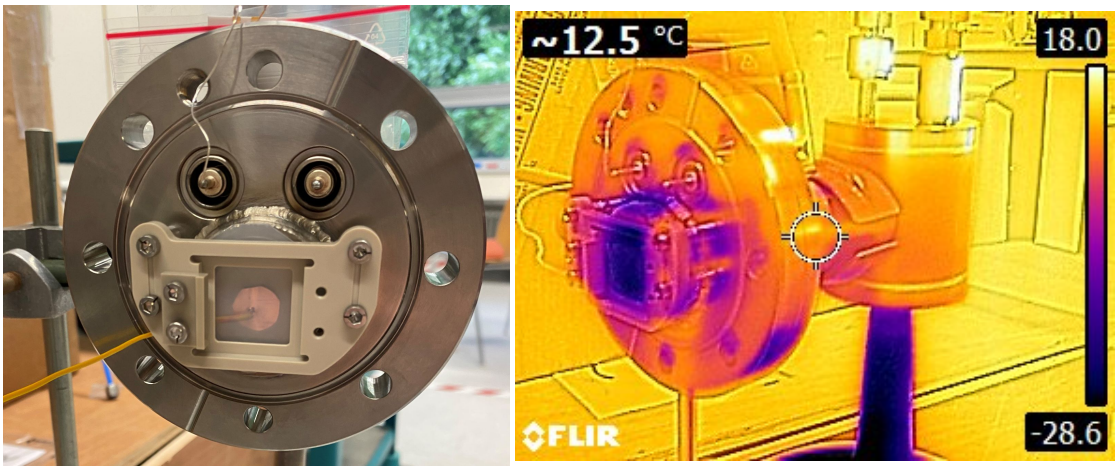

Figure 5.3: **Left:** Setup of the improved temperature measurement. The thermocouple wire is curled into a spiral between the cold plate and a copper plate to increase thermal conductivity. A plastic insulation was installed in order to apply some pressure, increase the thermal conductivity of the sensor, isolate from the surrounding air and improve thermal heat losses. **Right:** Picture of the Cryo Monitor setup with infrared camera. This picture is only suitable for a qualitative understanding of the heat transfer in the Cryo Monitor. The infrared camera used was only sensitive up to -20°C.

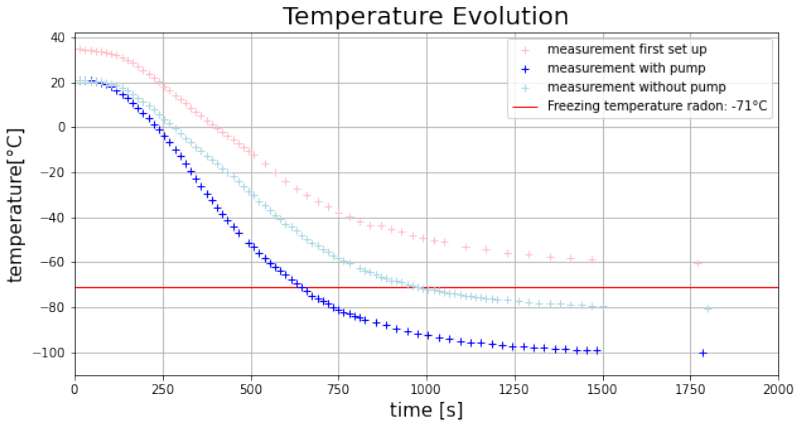

Figure 5.4: Temperature of the cold finger during a cold temperature test. Pink, cyan and blue correspond to the three, consecutively improved repetitions of the test. Red horizontal line shows the expected freezing radon temperature, the main goal to reach in this test. Each test was performed on ambient air exposure, and hence the thermal response of the system while being enclosed on V1 is expected to be even better.

5.3 Electrical connectivity and data acquisition

To check the connectivity of the electrical setup and to test the data acquisition system the americium source from subsubsection 4.3.2 was placed in front of the diode. In approximately 2.6 hours 33376 americium events were counted. This corresponds to an activity of 3.59 Bq. This result seems reasonable since it corresponds to a detection efficiency of about 36%. From the location of the ^{241}Am an ideal value of 50% is expected. However since the ^{241}Am activity was never certified, this measurement cannot give any accurate information on the diodes detection efficiency. This will be further elaborated in coming sections.

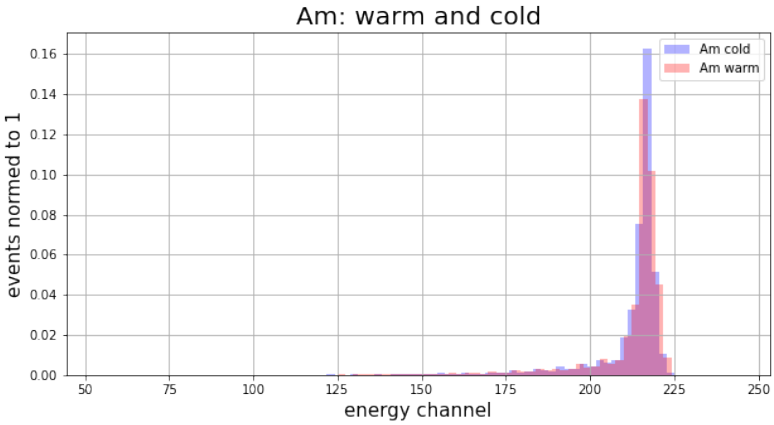

Figure 5.5: The americium spectrum was measured while cooling the cold finger (Am cold in blue) and without cooling (Am warm in red). No significant deviations can be observed.

The nitrogen tank is placed directly beside the electrics and thus could interfere with the measurement setup. To confirm

that the data is not changed due to the cooling process, data was taken also in cold conditions for 2 hours. Comparing both (see Figure 5.5) data sets we can observe that the spectrum did not change significantly. The americium peak is still at the same energy channel range and the same efficiency level.

5.4 Monte Carlo methods: geometrical efficiency and signal-shape

Monte Carlo methods are a broad class of computational algorithms that rely on repeated random sampling to obtain numerical results [21]. The underlying concept is to use randomness to solve problems that might be deterministic in principle. They are often used in physical and mathematical problems and are most useful when it is difficult or impossible to use other approaches.

In the following, this numerical approach is used to determine quantitatively or qualitatively the expected performance of the Cryo Monitor.

5.4.1 Diode geometrical efficiency factor

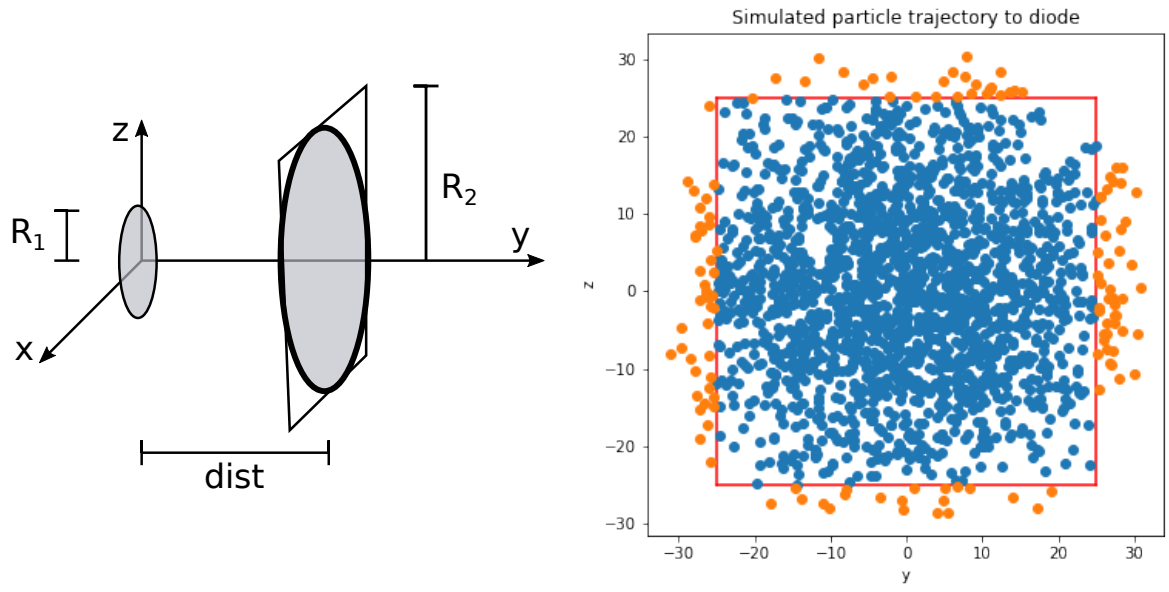

Figure 5.6: **Left:** x-y-z coordinates system used for the simulation. A circular cold-plate (with radius R_1) is sitting at the plane x-z (with y=0). A square diode with side of R_2 is situated in parallel, at y=*dist* (all distances in mm). **Right:** Distribution of alpha particles arriving at the diode-plane. Alpha trajectories reaching the diode (blue dots, when considering a square geometry, displayed in red) are used to compute the geometrical efficiency of the diode.

The Monte Carlo was performed to calculate the maximal efficiency of our Cryo Monitor, based on a pure geometrical factor. Two assumptions are taken:

- Alpha emission from radon decays is isotropic.

- Radon sits homogeneously on the cold plate.

The first assumption is very safe, however, the second assumption is quite idealistic. According to temperature simulations (see subsection 4.5) radon can freeze slightly outside the cold plate. This effect will decrease the efficiency in reality.

As seen in Figure 5.6, the Toy Monte Carlo only depends on the geometry of the instrument, that is the shape and size of cold-plate and diode, and the distance between the two. In this case a circular cold-plate of radius ∼2.5mm, a square diode of size ∼18mm, separated a distance of dist=2.5 mm is assumed.
The underlying uncertainty is the distance (dist) from the cold-plate and the diode. Taking into account an uncertainty in dist=2.5±1 mm, we end up with an efficiency of ε_g=38.36±0.82(stat)$^{+5}_{-4}$(sys)%.

Using the same code, and taking into account the geometry of the prototype detector from Wojcik and Zuzel [30](as presented in subsubsection 3.3.3), a total efficiency of ∼27.80±0.67% is obtained in contrast to the ∼34% as the authors claim.

5.4.2 Expected signal-shape for a cryogenic radon monitor

To learn more about the characteristics of the Cryo Monitor a very simple Toy Monte Carlo model was developed to reproduce the collection of events dependent on time. This 2D model assumes that a radon particle can be created anywhere in the detector chamber. They move at constant speed, can't leave the chamber and get reflected once they hit a wall. The trajectory of the particle is randomised due to interaction with the carrier gas (modelled with a Gaussian function centred at the particles trajectory). Each radon particle has a likelihood to decay. When the particle reaches the cold plates surface it stays frozen until decay. The decay is then seen by the diode with a likelihood of 100%.

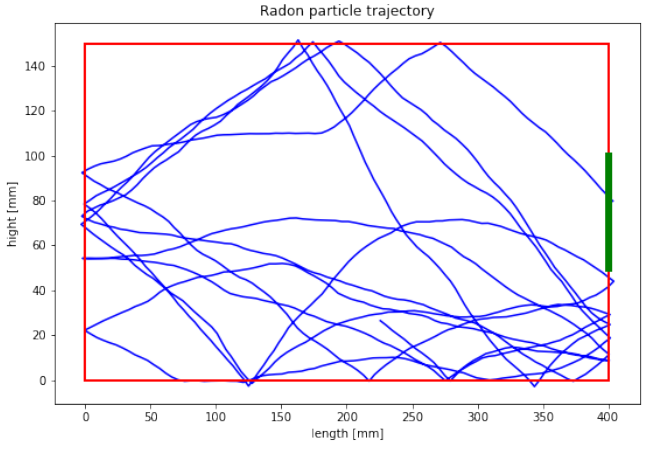

Figure 5.7: Simulated trajectory of 1 particle. Simulation was performed in loops of 1 second, where the particle speed as 5e-3 m/s. At each iteration, a random fluctuation, modelled with a gaussian function with $\sigma = 2\pi/100$, was added. The particle reaches the diode (shown in green, centered in the most right end wall of the diode).

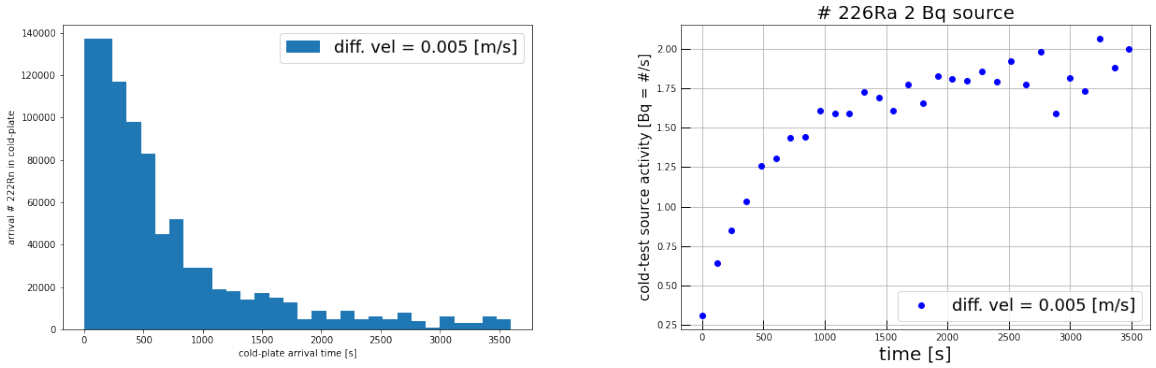

Figure 5.8: **Left:** Time dependent evolution of arriving particles onto the cold plate. Number of ^{222}Rn particles normalised to the equilibrium for a 2 Bq ^{226}Ra source ($\sim$1e6 particles). Time t=0 corresponds to the time the cold-plate reaches radon freezing temperature. **Right:** Expected α emission on the diode, in the same time units (geometrical and diode detection efficiencies not taken into account).

Assuming a length of 400 mm, a height of 150 mm for the monitor and a total (1D-)surface of the diode of 50 mm, the in-growth signal-shape for radon particles moving at a speed of 0.005 m/s can be reproduced. At each time iteration each particle trajectory can be randomly deviated due to scatters with the carrier gas atoms. The outcoming trajectory angle is defined by a Gaussian distribution around the incoming trajectory angle with a σ=$\frac{2\pi}{100}$ deg.

With this simple model that depends only on the diffusion speed we can reproduce the expected signal-shape for a cryogenic radon monitor as can be seen on the left of Figure 5.8. In an initial in-growth phase radon accumulates on the cold plate. Based on this model, the total length of the initial in-growth phase is a function of the median speed radon diffuses inside the monitor. Following the in-growth phase is a stable signal.

6 Cryo Monitor performance

In this section I will present a selection of measurements that have been taken with the Cryo Monitor and evaluate the Cryo Monitors performance. I will begin with the background measurement and from this the minimal detectable activity (MDA) will be calculated. Next, I will prove that the Cryo Monitors operation principle is working properly. Then the dependence of carrier gas type and pressure will be further examined. Last the energy resolution is investigated closer.

6.1 Background, efficiency and ^{222}Rn minimal detectable activity

Indispensable for all measurements is a good estimation on the background of the Cryo Monitor. With this information the MDA can be determined. There are two independent components that cause background.

First component is caused by a combination of alpha-emitting impurities in the semiconductor diode (especially in the active surface layer) and cosmic ray events. For instance cosmic muons can easily enter through the building and hit the diode, thereby depositing energy in the same energy window a ^{222}Rn decay is expected. This background was measured by taking data while V1 was under pumping (note that with the Isolde sample still inside, emanated ^{222}Rn should be pumped out before reaching the cold plate). If V1 is pumped no emanated radon from Isolde or the material of the chamber should be detected by the diode. The background signal in the ^{222}Rn region of interest is A_{B1} = (15±4) counts per day (cpd). Data was taken for 8 hours and the same energy cuts were used for the background events as they were in the later measurements.

The second source of background is caused by permanent emanation of ^{222}Rn inside the V1 chamber, emanating for instance from welds, valves or the not electropolished stainless steel pipe. Ideally, this measurement should be performed without the radon source inside the volume and while cooling the cold finger. However due to the long half-life of radon, the chamber would have to emanate for 2 weeks before taking data. Because of time restrictions this value was estimated by the emanation of stainless steel of (150 $\pm$ 100) μBq/m^2[18] and the total surface of the Cryo Monitor of (0.07567 $\pm$ 0.00002)m^2. The estimated background caused by emanation is A_{B2}=(0.98$\pm$0.65) cpd. Subdominant with respect to A_{B1}.

The total background was calculated by summing up both backgrounds A_B=$A_{B1} + A_{B2}$=16$\pm$4 cpd. The MDA was estimated at 90% confidence level (CL), by integrating a Poisson distribution with a mean value of 16 cpd. An upper fluctuation of 21 cpd is excluded at this CL (21^{90CL}_{cpd}), therefore hinting to the presence of an additional source (see Figure 6.1).

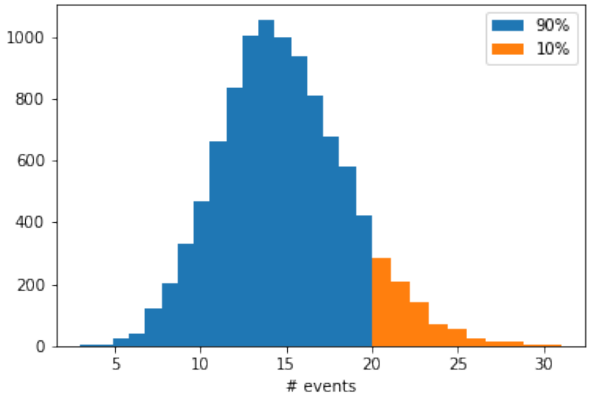

Figure 6.1: The Poisson distribution is centred at A_B=16 cpd. The interval between 0 and 21 includes events caused by the total background with a likelihood of 90%. 10000 events were used to construct this distribution.

Additionally, the absolute detection efficiency ε has to be considered. As will be explained in the following sections ε_{max} was empirical determined to be $(22.46 \pm 0.38)\%$. Since additional 5 events above background indicate an additional source the minimal detectable activity, assuming maximal detection efficiency ε_{max}, can be written as following:

$$A_{min} = \frac{5cpd}{day \cdot \varepsilon_{max}} = (0.26 \pm 0.12) mBq. \tag{10}$$

The error ΔA_{min} was estimated with the uncertainty of the detection efficiency $\Delta\varepsilon_{max}$ and $\Delta 5$ cpd=$\sqrt{5}$ cpd:

$$\Delta A_{min} = A_{min} \cdot \sqrt{\left(\frac{\Delta 5cpd}{5cpd}\right)^2 + \left(\frac{\Delta\varepsilon_{max}}{\varepsilon_{max}}\right)^2} \tag{11}$$

Taking into account the active volume of the detection chamber (1.434 l) the minimal detectable concentration of ^{222}Rn is (0.181±0.083)Bq/m^3.

6.2 Freezing measurement

The Isolde sample (see subsubsection 4.3.2) was introduced inside the radon monitor. The chamber was filled with a small amount of helium(∼2.5 mbar) and given time for the activity of the source to grow and approach the equilibrium activity (see section 3).

For all measurements the experimental activity for ^{222}Rn was calculated and compared with the theoretical activity from subsubsection 3.2.3. Events in a selected energy channel window for each peak are summed up and compared with the theoretically expected events in that time. The selected region is marked in purple-orange-grey for ^{222}Rn-^{218}Po-^{214}Po respectively (Figure 6.2). The energy windows were set after each measurement to achieve the best possible selection. For all measurements a time cut was also applied to consider only the measurement after the plateau signal region described in subsubsection 5.4.2 was reached.

Hereafter, we refer as cold or warm measurements, for data acquisition periods in which the cold plate was kept at LN_2 temperatures or at ambient temperature respectively.

In Figure 6.2 we see a warm and cold run with different measurement times after the source emanated for 16 days, hence we expect a activity of nearly 95 % of the equilibrium activity. The data for the warm measurement was taken for ∼12 hours and for the cold run for only ∼ 2 hours. In the cold run we observe significantly more events within the energy windows of the 3 isotopes mentioned. In the warm run the detection efficiency of $\varepsilon_{200}^{warm} = (0.08 \pm 0.01)\%$ is vastly lower than the cold runs efficiency of $\varepsilon_{200}^{cold}(14.33 \pm 0.30)\%$. This increase can only be caused by collection of radon atoms on the cold plate, proving that the cryo-pump of the cold-plate is working.

In the following, the dependency of the trapping efficiency on the helium carrier gas pressure is studied.

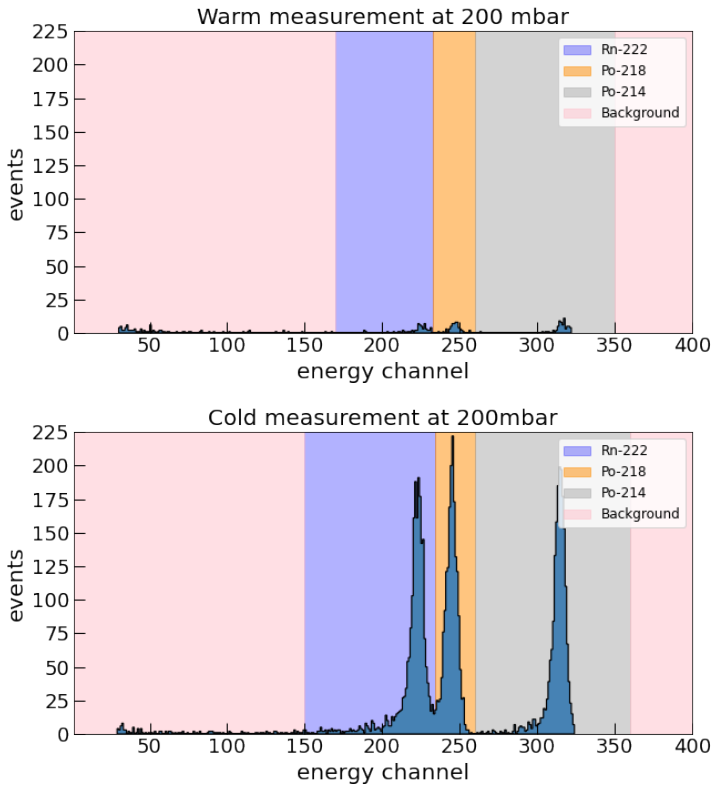

Figure 6.2: **Top:** Measurement at 200 mbar helium without cooling for an exposure time of ∼ 12h **Bottom:** Measurement at 200 mbar of helium with cooling at a exposure time of ∼ 2h. The peak selection is marked in colour. Significantly more events are visible in the cold measurement, thereby proving the successful collection of ^{222}Rn on the cold plate. The radon emanation level was at (1.945±0.002) Bq.

6.3 ^{222}Rn cold plate collection time

The Monte Carlo simulation in subsubsection 5.4.2 suggested that the Cryo Monitors signal starts with initial in-growth phase until a stable activity (equilibrium) is reached. Henceforth the time until equilibrium is called *collection time*. Since the collection time in the simulation was only dependent on the speed of the radon particles, it is expected that higher carrier gas pressures slow down the radon particles and thereby require longer collection times. To further study the in-growth signal tests were performed for 4 different pressures and two different gas types as will be covered below. Self-explanatory all tests hereafter were performed while cooling the cold finger.

6.3.1 Influence of helium pressure on the ^{222}Rn collection efficiency

First the Cryo Monitor was tested using four different pressures of helium as a carrier gas. The measurement time differed according to the time needed to reach a stable signal from the diode.

Figure 6.3 displays the events measured in the energy window of ^{222}Rn (red), ^{218}Po (blue) and ^{214}Po (light-blue) as a function of time after the cold finger is put in LN_2 using Helium as carrier gas at time zero. Each time bin is 400 seconds. The figure at top-left, top-right, bottom-left and bottom-right correspond to helium pressures of 2.5, 100, 200 and 400 mbar respectively. At each measurement Isolde was enclosed inside the detection chamber V1, with an activity of ∼95% of the equilibrium activity.

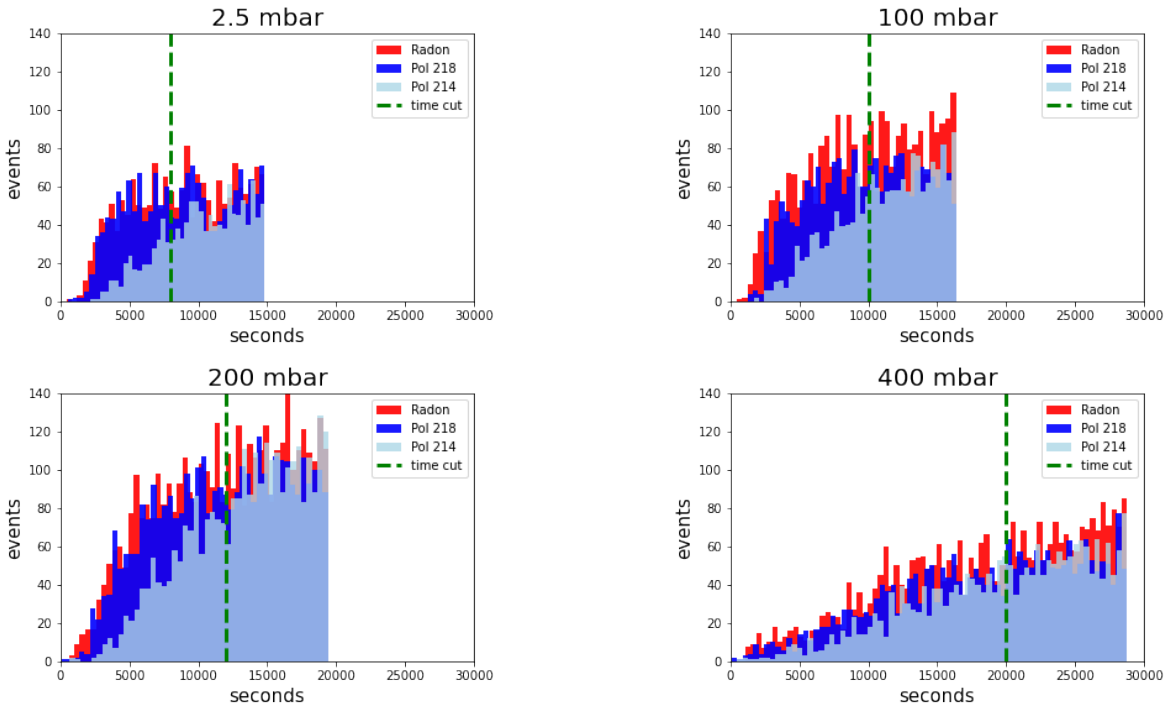

Figure 6.3: Time evolution of ^{222}Rn, ^{218}Po, and ^{214}Po events dependent on pressures of helium. The bin size is 400 seconds. Different measurement times were used to reach saturation in each measurement. The dashed green line signifies after which time data was used to calculate the experimental efficiencies.

In Figure 6.3 it can be observed how the slope of the in-growth signal flattens with applied pressure. A pressure of 2.5 mbar results in the shortest collection time of only 3 hours. In contrast the measurement with the highest pressure of 400 mbar did not even reach full saturation after 8 hours of measurement time.
As expected, we observe that radon events reach saturation first and the polonium events build up last.

6.3.2 Influence of nitrogen pressure on the ^{222}Rn collection efficiency

To study the dependence on carrier gas type, the measurements from subsubsection 6.3.1 were repeated at pressure levels 2.5 mbar, 100 mbar, 150 mbar and 200 mbar with nitrogen as a carrier gas. After gaining some experience with the helium data, the measurement times for lower gas pressure were extended to ensure saturation.

As before Figure 6.4 displays the events measured in the energy window of ^{222}Rn (red), ^{218}Po (blue) and ^{214}Po (light-blue) as a function of time after the cold finger is put in LN_2 at time zero. The figure at top-left, top-right, bottom-left and bottom-right correspond to helium pressures of 2.5, 100, 150 and 200 mbar respectively. At each measurement Isolde was enclosed inside the detection chamber V1, with an activity of ∼84% at 2.5 mbar, ∼90% at 101 mbar, ∼92% at 200 mbar and ∼93% at 400 mbar of the equilibrium activity. As before the in-growth curve flattened and collection times increased with pressure. Overall, more events were detected with nitrogen as a carrier gas.

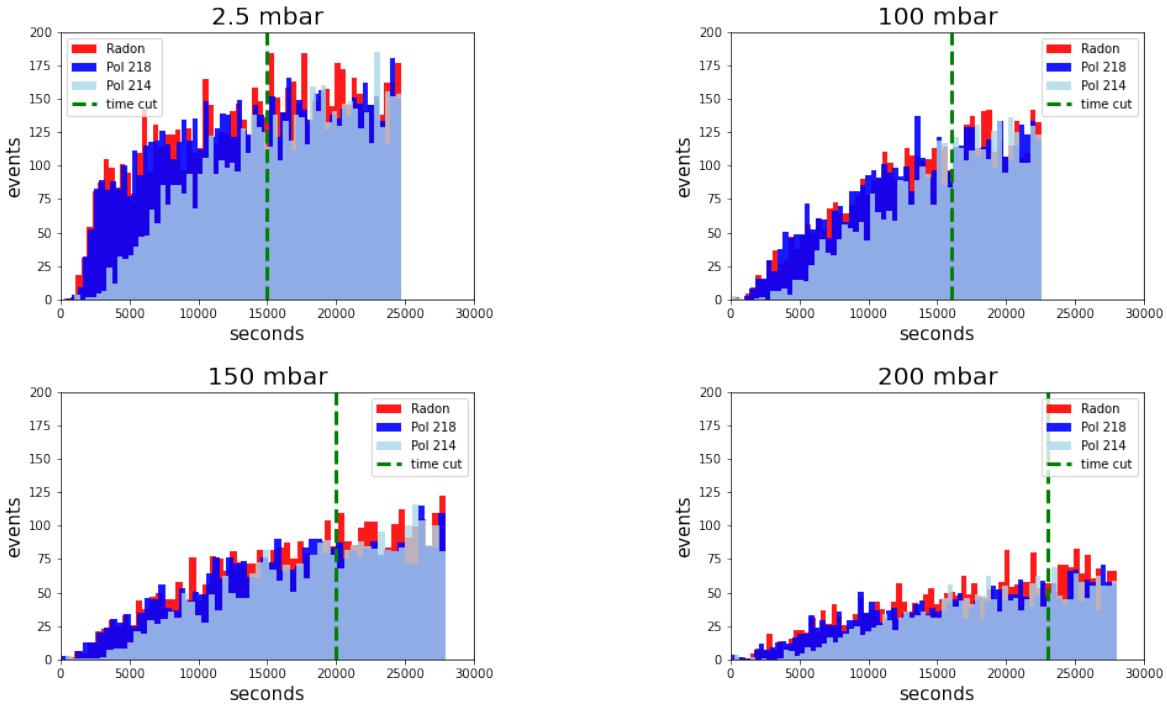

Figure 6.4: Time evolution of ^{222}Rn, ^{218}Po, and ^{214}Po events dependent on pressures of nitrogen. The bin size is 400 seconds. Different measurement times were used to reach saturation in each measurement. The dashed green line signifies after which time data was used to calculate the experimental efficiencies.

6.4 Carrier gas pressure dependence of the collection efficiency

Another important parameter for the application of the Cryo Monitor is the optimal carrier gas pressure. For every measurement the collection efficiency with respect to their theoretical activity as described in subsection 6.2 was calculated. The efficiency $\varepsilon_{gas}^{pressure}$ can be calculated by dividing the experimentally measured activity A_{exp} with the theoretical expected activity A_{theo}:

$$\varepsilon = \frac{A_{exp}}{A_{theo}}. \tag{12}$$

The errors calculation for the efficiency $\Delta\varepsilon$ was calculated using following equation,

$$\frac{\Delta\varepsilon}{\varepsilon} = \sqrt{\left(\frac{\Delta A_{ex}}{A_{ex}}\right)^2 + \left(\frac{\Delta A_{theo}}{A_{theo}}\right)^2}. \tag{13}$$

Whenever not classified ε refers to absolute detection efficiency in the cold state. The experimental measured A_{exp} activity and its error ΔA_{exp} were estimated with following equations:

$$\begin{aligned} A_{exp} &= \frac{Events}{t}, \\ \Delta A_{exp} &= \frac{\sqrt{Events}}{t}. \end{aligned} \tag{14}$$

The theoretical estimated activity was calculated by averaging the activity at beginning A_{begin} of the measurement and end A_{end} of the measurement as obtained by Equation 6.

$$\begin{aligned} A_{theo} &= \frac{A_{begin} + A_{end}}{2}, \\ \Delta A_{theo} &= \sqrt{\frac{(A_{theo} - A_{begin})^2 + (A_{theo} - A_{end})^2}{2}} \end{aligned} \tag{15}$$

To evaluate whether saturation was reached the ratio of ^{218}Po/^{222}Rn was used. For an established equilibrium the ration should be 1. The ratio ^{218}Po/^{222}Rn and its error Δ^{218} Po/^{222}Rn was calculated as following:

$$^{218}Po/^{222}Rn = \frac{Events_{^{218}Po}}{Events_{^{222}Rn}} = \frac{\#_{^{218}Po}}{\#_{^{222}Rn}} \tag{16}$$

with # being the number or events integrated in the corresponding energy region

$$\Delta^{218}Po/^{222}Rn = \sqrt{\left(\frac{\sqrt{\#_{^{218}Po}} \cdot \#_{^{218}Po}}{\#_{^{222}Rn}}\right)^2 + \left(\frac{\sqrt{\#_{^{222}Rn}}}{\#_{^{222}Rn}}\right)^2} \tag{17}$$

Where poisson errors are considered for #.

6.4.1 Collection efficiency for different pressures of helium as a carrier gas

For helium the results are gathered in Table 1. The highest collection efficiency $\varepsilon_{200}^{He} = (14.33 \pm 0.30)\%$ was observed for 200 mbar, indicating an optimal operating pressure for helium as a carrier gas. The pressure error has been estimated according

to the data sheet of the RPT 100 vacuum gauge (see subsubsection 4.2.1). The green dashed line in Figure 6.3 marks after which time data was used to calculate the efficiency. The line was set according to criteria of saturation and sufficient length of measurement time.

Pressure of helium [mbar]	Integrated time [s]	Efficiency[%]	Ratio of ^{218}Po/^{222}Rn
2,5 $\pm$ 5	6820	8.16 $\pm$ 0.25	0.932 $\pm$ 0.042
100 $\pm$ 1	4380	11.29 $\pm$ 0.37	0.816 $\pm$ 0.040
200 $\pm$ 1	7440	14.33 $\pm$ 0.30	0.854 $\pm$ 0.028
400 $\pm$ 2	8800	8.78 $\pm$ 0.23	0.777 $\pm$ 0.030

Table 1: Absolute collection efficiency of ^{222}Rn and the measured count ratio of ^{218}Po/^{222}Rn for four different helium pressures. The low ratio of ^{218}Po/^{222}Rn for 400 mbar indicates that saturation was not yet reached. Contrary, the measurement with 2.5 mbar achieved almost saturation.

6.4.2 Collection efficiency for different pressures of nitrogen as a carrier gas

In Table 2 the efficiencies of nitrogen as a carrier gas are collected. The highest efficiency was observed for the lowest pressure of nitrogen $\varepsilon^N_{2.5} = (22.46 \pm 0.38)\%$. Pressure error and data were obtained as described for the helium measurement.

Pressure of nitrogen [mbar]	Integrated time [s]	Efficiency[%]	Ratio of ^{218}Po/^{222}Rn
2,5 $\pm$ 0.1	9720	22.46 $\pm$ 0.38	0.918 $\pm$ 0.022
101 $\pm$ 1	6560	16.59 $\pm$ 0.37	0.971 $\pm$ 0.031
150 $\pm$ 1	7960	10.53 $\pm$ 0.26	0.850 $\pm$ 0.031
200 $\pm$ 1	5080	8.59 $\pm$ 0.29	0.832 $\pm$ 0.043

Table 2: Absolute collection efficiency of ^{222}Rn and the measured count ratio of ^{218}Po/^{222}Rn for four different nitrogen pressures. ^{218}Po/^{222}Rn ratios indicate that all measurements were close to saturation.

6.4.3 Carrier gas pressure dependence on the collection efficiency

Figure 6.5 shows the experimental measured efficiencies as a function of pressure for both helium and nitrogen. The efficiency merely expected from the geometries of the cold plate and diode and its 1 σ error band is plotted as a green line with a transparent green bar. A maximum data point is observed at pressure equal 200 mbar and 2.5 mbar for helium and nitrogen respectively. An absolute maximum can be expected between pressures 200-400 and $\sim$0-2.5 mbar for each gas respectively, however more data points are needed to assure this statement.

In general, nitrogen seemingly provides higher efficiencies between pressures of 2.5-100 mbar and helium after 100 mbar. However, both maximum efficiencies are factor $\sim$2 below the geometrical efficiency ε_g=38.36 $^{+5}_{-4}$(sys)%.

Still, from the measurements conducted here the optimal operation conditions is using nitrogen as carrier gas at a pressure of 2.5 mbar.

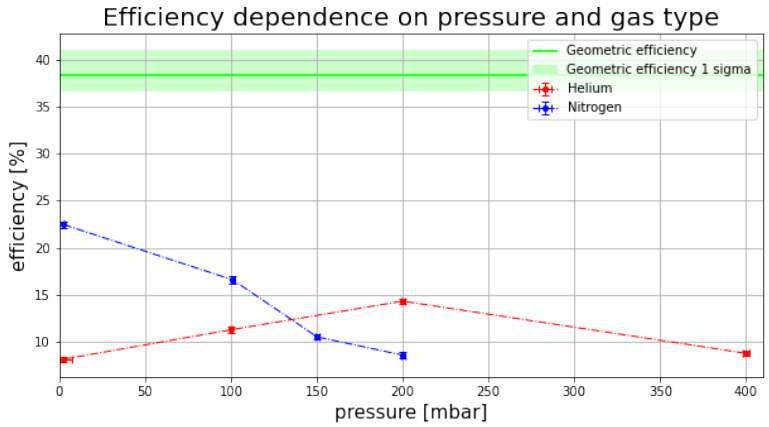

Figure 6.5: Freezing efficiency as function of pressure of the carrier gas. The green line represents the maximal expected efficiency from a geometrical view and light green bar the 1-σ range. Helium measurements are shown in red and nitrogen measurements in blue. Two dashed lines join the the data points of the same carrier gas for better visualisation

6.5 Energy resolution

A good energy resolution helps to distinguish the different energy peaks of the isotopes. For higher pressures the ^{222}Rn peak got contaminated with low energy events from the ^{218}Po peak. To obtain a better understanding of the energy resolution of the Cryo Monitor, three Crystal Ball functions were fitted on the three isotope peaks from the 200 mbar helium cold measurement. The Crystal Ball function is defined as follows:

$$f = f(x,\alpha,n,\bar{x},\sigma) = N \cdot \begin{cases} exp\left(-\frac{(x-\bar{x})^2}{2\cdot\sigma^2}\right), & \text{for} \quad \frac{x-\bar{x}}{\sigma} > -\alpha \\ A\cdot\left(B-\frac{x-\bar{x}}{\sigma}\right)^{-n}, & \text{for} \quad \frac{x-\bar{x}}{\sigma} \leq -\alpha \end{cases} \tag{18}$$

With

$$\begin{aligned} A &= \left(\frac{n}{|\alpha|}\right)^n \cdot exp\left(-\frac{|\alpha|^2}{2}\right), \\ B &= \frac{n}{|\alpha|} - |\alpha|, \\ N &= \frac{1}{\sigma(C+D)}, \\ C &= \frac{n}{|\alpha|}\cdot\frac{1}{n-1}\cdot exp\left(-\frac{|\alpha|^2}{2}\right), \\ D &= \sqrt{\frac{\pi}{2}}\cdot\left(1+erf\left(-\frac{|\alpha|}{\sqrt{2}}\right)\right), \end{aligned}$$

and α, n,$\bar{x}$ and σ which are fitted with the data. erf is the error function. The Crystal Ball function is commonly used to model various lossy processes in high-energy physics. Each Crystal Ball function consists of a Gaussian core portion and a

power-law low-end tail, below a certain threshold. In the case of the Cryo Monitor, the low-end energy tail is caused as a result of alpha particles losing energy by bumping into other gas molecules on the way to the diode and the dead layer of the diode. For the measured energy spectra, the length of the low energy tail differed with the pressure of carrier gas. In was observed that increasing the pressure resulted in widened peaks and an elongated low energy tail as can be seen in Figure 6.6.

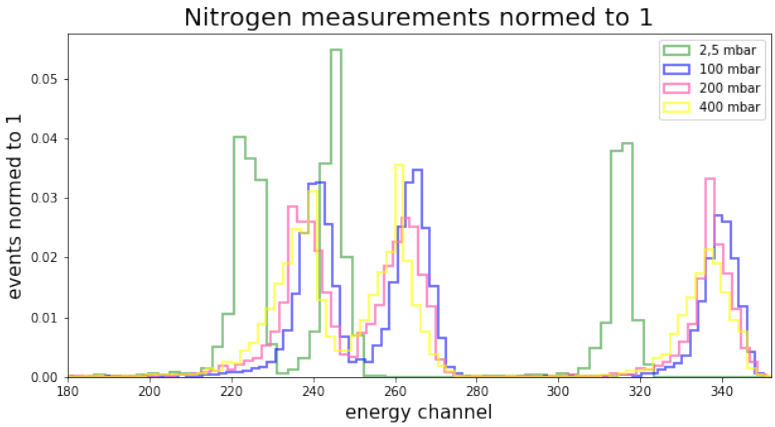

Figure 6.6: Comparison of the width of the nitrogen peaks. For reasons of comparability the events of each spectrum are normed to 1. Higher pressures result in broader peaks and a longer low-energy tail

The fit function is three Crystal Ball functions $f_i = f(x, \alpha_i, n_i, \bar{x}_i, \sigma_i)$, $i \in [1,2,3]$, summed up:

$$f_{Fit} = f_1 + f_2 + f_3. \tag{19}$$

Figure 6.7 displays the three isotope peaks in logarithmic scale. The red dashed line is the fit of the sum of three Crystal Ball functions f_{Fit}. In grey, orange and light-blue single Crystal Ball functions f_i were fitted to the peaks of ^{222}Rn,^{218}Po and ^{214}Po respectively.

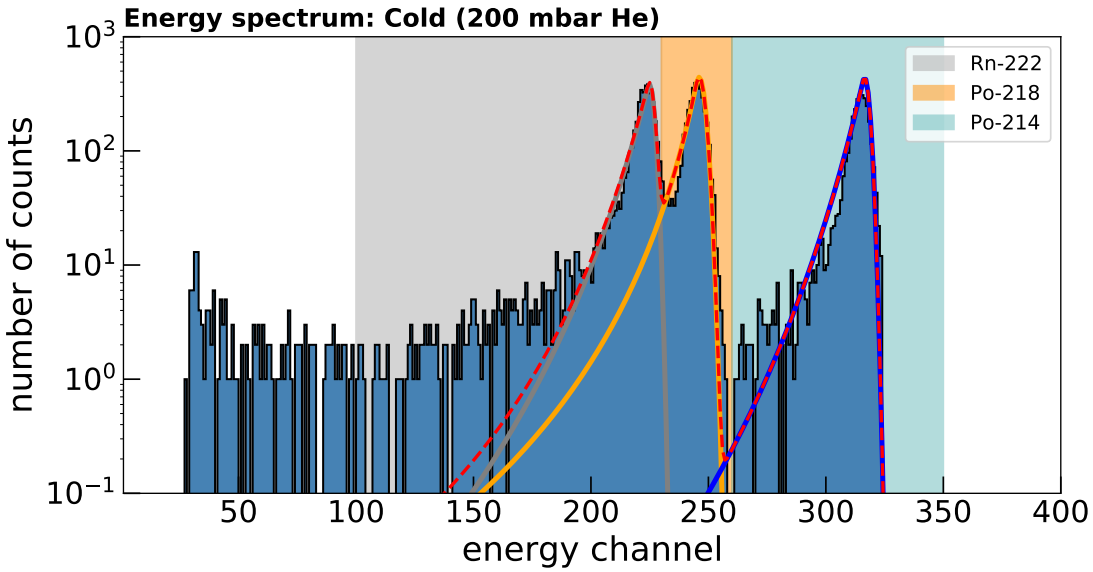

Figure 6.7: Cold spectrum for 200 mbar of helium with Crystal Ball fit. The dashed red line is the fit of the sum of three Crystal Ball functions to the three isotope peaks. In grey, orange and light-blue single Crystal Ball functions were fitted to the peaks of ^{222}Rn,^{218}Po and ^{214}Po respectively.

The energy resolution for each peak was estimated with the σ parameter from the Crystal Ball function fit:

$$\Delta E^i_{res} \equiv \sigma^i_p. \tag{20}$$

With i and p referring to the isotope peak and the pressure of the carrier gas. In Figure 6.7 it can be seen that the Crystal Ball function fits much better to the data recorded, than a simple Gaussian function. Still a Crystal Ball fit doesn't fully describe the measured spectrum. σs of the fit of three Gaussian's were compared with the fitparameter of the three Crystal Ball functions. They were consistent within their error, therefore the dependence of the Crystal Ball functions tail on the width of the peaks is negligible. A goodness of fit is redundant due obvious deviation between fit and measurements. The energy resolution is averaged by the three resolutions obtained from the three fitted Crystal Ball fits (under the assumption that the energy resolution is constant for all three peaks):

$$\begin{aligned} E_{res} &= \frac{E^{Rn222}_{res} + E^{Pol218}_{res} + E^{Pol214}_{res}}{3} = (0.3143 \pm .0.0023(stat) \pm 0.09(sys))MeV. \\ \Delta E_{res}(stat) &= \sqrt{\frac{1}{3} \cdot \left((E_{res} - E^{Rn222}_{res})^2 + (E_{res} - E^{Pol218}_{res})^2 + (E_{res} - E^{Pol214}_{res})^2 \right)} \\ \Delta E_{res}(sys) &= \frac{1}{3} \cdot \sqrt{(\Delta E^{Rn222}_{res})^2 + (\Delta E^{Pol218}_{res})^2 + (\Delta E^{Pol214}_{res})^2} \end{aligned} \tag{21}$$

An energy resolution of $(0.3143 \pm .0.0023(stat) \pm 0.0001(sys))$ MeV is determined for the spectrum of 200 mbar helium pressure. The statistical error was derived from the variance of the three measurements. For each σ there is a systematic error that stems from the fitting of the energy calibration (see subsubsection 6.5.1). For higher pressures, lower resolutions are expected due to wider peaks and more pronounced low energy tails.

6.5.1 Energy calibration

The channel to energy calibration was done by plotting the theoretical energy of the decays E against the channel C where the respected peak was observed. Because the energy had to be calibrated every measurement again only three measurement points were available for a fit. Following fit functions was used:

$$C(E) = a \cdot E + b \tag{22}$$

The fitparamter were determined to be a=38 ± 11 channel·MeV^{-1} and b=14 ± 6 channel. From Equation 22 the energy calibration and its error can be derived:

$$\begin{aligned} E(C) &= \frac{C-b}{a}, \\ \Delta E(C) &= \sqrt{\left(\frac{(C-1)\cdot \Delta b}{a}\right)^2 + \left(\frac{(C-b)\cdot \Delta a}{a^2}\right)^2} \end{aligned} \tag{23}$$

Since only three measurement points were fitted for the energy calibration, this calculation is only used for a qualitative understanding of the Cryo Monitor and has no further significance.

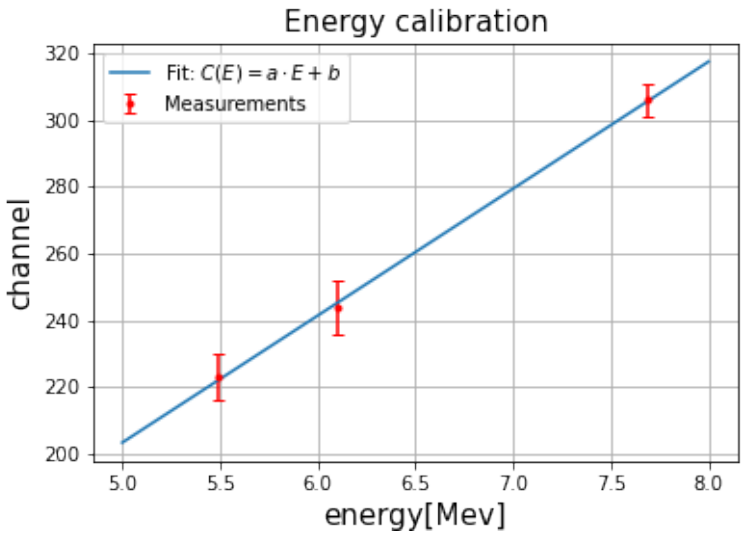

Figure 6.8: Energy calibration: Channel vs. theoretical decay energy are plotted for the cold measurement at 200 mbar. A line fit was used to describe the three data points

7 Summary and Conclusions

My main objective of this Bachelor thesis was to build and operate a new detector for ^{222}Rn. Many international research projects require an extremely low background to reach desirable sensitivities. The XENONnT dark matter search experiment was able to lower background to a level in which the permanent ^{222}Rn emanation is the dominant source. To lower the background caused by ^{222}Rn emanation further, materials are screened and selected for their radon content. Even though there are many different radon detectors available, they either lack in sensitivity or applicability. Therefore, a Cryo Monitor was studied for its potential use in low background screening facilities. The Cryo Monitor is anticipated to be easier to operate, because it only requires liquid nitrogen (LN_2), resistant to high pressures and able to detect activities as low as a few mBq.

In subsection 7.1 I will conclude all measurements and in subsection 7.2 I will give an outlook on potential improvements to the Cryo Monitor setup.

7.1 Experimental results and future work

It could be proven that the Cryo Monitor actually is able to freeze radon on a cold plate, thereby dragging radon close to the diode and improving the ^{222}Rn collection efficiency of the diode significantly.

The background is one of the most important parameters of the Cryo Monitor. Due to of time restrictions for this thesis the background caused by permanent emanation of ^{222}Rn inside the chamber was not measured and instead estimated from the detectors material and inner surface. A total background of $A_B = 16 \pm 4$ cpd was determined. Future measurements include a measurement of the background caused by permanent emanation of ^{222}Rn inside the chamber A_{B2}. For this measurement the detection chamber should be filled with the carrier gas pressure of maximum detection efficiency and then given at least two weeks to emanate. This time delay corresponds to time the radon source was given for emanation before measuring. The background measurement should be performed as a cold run.

The background influences the minimal detectable activity (MDA) of the Cryo Monitor. The detector achieves a MDA of about $\sim (0.26 \pm 0.12)$ mBq. In comparison the prototype detector developed by M.Wojcik and G.Zuzel [28] achieved a MDA of $\sim (0.8 \pm 0.24)$ mBq. The observation of a lower MDA in the Cryo Monitor setup at the MPIK comes as no surprise. A smaller detection chamber has less background and therefore is able to provide lower MDAs. Furthermore, could a careful selection of materials reduce the background and therefore improve the MDA even more.

Another important parameter for a low-level detector is its absolute detection efficiency. The absolute detection efficiency can be written as $\varepsilon = \varepsilon_e \cdot \varepsilon_g \cdot \varepsilon_d$. Where ε_c is the efficiency of radon collection on the cold plate, ε_g is the efficiency-based geometries and ε_d depends on the detection probability of the diode. For the geometry presented ε_g=38.36$\pm$0.82(stat)$^{+5}_{-4}$(sys)% was determined by a Monte Carlo simulation. The maximum absolute efficiency observed is $\varepsilon^N_{2.5}$ =(22.46$\pm$0.38)%for $\sim$2.5 mbar of nitrogen. The deviation from ε_g is probably caused by the other efficiency factors: either ε_c or ε_d. The diode was never investigated with a calibrated α-source thus ε_d is not determined by now. A calibration of the diode is planned. For

this a radioactive α-source with a known activity will be placed in front of the diode. With regard to the geometric factor the efficiency of the diode ε_d is then measured. Afterwards ε_c is derived. As soon as the detection efficiency of the diode ε_d is experimentally measured the total collection efficiency ε_c is known as well. If ε_c is very low, water might have been frozen on the cold plate, effectively preventing radon to accumulate. Possible but not very likely is that the cold plate didn't reach radon freezing temperature. The latter was already refuted by both a temperature simulation and a measurement while the cold plate was on air.

Another important aspect is the energy resolution of the Cryo Monitor. For higher gas pressures the alpha peaks broadened and moved to lower energies. This effect might is related to alphas losing energy on their way from the cold plate to the diode, by colliding with gas molecules. At higher pressures more molecules are available for collision, hence the peaks develop a low-energy tail of particles that lost part of their energy in collision. Exemplary for a pressure of 200 mbar of helium the energy resolution of $(0.3143 \pm .0.0023(stat) \pm 0.0001(sys))$ MeV was determined. Nevertheless, the energy resolution will be confirmed for the best operational pressure and carrier gas type (currently nitrogen at a pressure of 2.5 mbar) with multiple measurements in the future.

To find the optimal operation conditions for the Cryo Monitor measurements at different pressures of nitrogen and helium were performed and compared. Helium measurements showed maximal detection efficiency at 200 mbar of helium and less efficiency for higher and lower pressures. Nitrogen showed however a decline in efficiency with increasing pressure. A maximum data point is observed at pressure equal 200 mbar of $\varepsilon^{He}_{200} = (14.33 \pm 0.30)\%$ and 2.5 mbar of $\varepsilon^{N}_{2.5} = (22.46 \pm 0.38)\%$ for helium and nitrogen respectively. In contrast, the detector by Wojcik and Zuzel[30] provided similar efficiencies with different helium pressures. They also observed a decline of efficiency with pressure for nitrogen as a carrier gas. From these measurements it can be concluded that nitrogen is a better choice as a carrier gas for the Cryo Monitor. To verify an optimal pressure more data will be taken in the region of interest between $\sim$0 and 2.5 mbar.

Tests showed that the collection time needed to reach stable activity is strongly dependent on the carrier gas pressure for both gas types. As an example helium at 2.5 mbar reached equilibrium between ^{222}Rn absorption and desorption after only $\sim$ 3 hours, but for 400 mbar helium the collection is not even completed after $\sim$ 8 hours. This flattening of the in-growth curve of ^{222}Rn events is even stronger with nitrogen. These results agree with the Wojcik and Zuzel's detector [30] in which the highest pressures also demanded longer collection times. This effect is related to the diffusion speed of radon in gas. As has been shown by a simple Monte Carlo simulation the in-growth time until a stable signal is reached is only dependent on the speed of radon atoms moving. Gas molecules slow down and scatter at the radon particles, thereby extending the collection time. What cannot be explained at the moment is why the collection times observed with the Cryo Monitor are much longer than the collection times observed by Wojcik and Zuzel. For comparison, the longest collection time observed is only 100 minutes (at a pressure of 400 mbar of helium). For a Cryo Monitor in operation, shorter collection times would be most desirable. Hence this effect will be further studied.

While developing the Cryo Monitor setup presented here, different locations of the radon source were tested. A first attempt was to locate the radon source in an isolated chamber connected to the main volume. Each measurement proceeded as

following: The chamber was filled up with helium to 1 bar and closed. After given time for emanation the radon chamber was opened into Volume 1, which was in a state of vacuum. The cold measurement was done as described for the Cryo Monitor final setup.
This attempt was not successful. Radon could be frozen but the efficiencies were lower than 1%. The location of the radon source outside the main detection chamber was simply not sufficient for effective diffusion of radon. This test should be repeated with the optimal operation conditions found out in this bachelor thesis.

After commissioning and evaluating the devices performance, potential improvements for the Cryo Monitor became apparent. In the next section these improvements are presented.

7.2 Potential improvements

In general differences in performance between the Cryo Monitor build at MPIK and the Cryogenic Monitor[30] were anticipated since their setup differ. Contrary to the prototype, the Cryo Monitor is smaller and cools the cold plate with a copper rod dipped in LN_2. This results in a weaker cooling power and therefore lower collection efficiency. Additionally, a water trap should have further increased the collection efficiency in the prototype setup. From these differences in setup, potential improvements can be deduced.

There are two different types of improvements that can be done to the Cryo Monitor I've been operating. The first type of improvements allows better monitoring of the pressure and temperature of the setup. The second type should actually improve the performance of the device itself.

First it might be useful to install a temperature sensor, that measures the cold plates temperature. This sensor, probably a thermocouple, should be read out during every measurement. Also, the temperatures of different parts of the setup should be checked. After taking data for the cold run in helium, monitoring of the pressure was achieved. However until now, it was only used to confirm the absence of a leak while cooling. In the future the pressure should be simultaneously read out with every measurement. It would be useful to be able to alter the distance between cold plate and diode and to exchange the cold plate size/shape. With alterations the geometrical factor could be understood better.

There are several improvements that could potentially enhance the Cryo Monitors performance. First the the background can be reduced by carefully selecting the materials used to build the Cryo Monitor. For instance the stainless steel pipe that is surrounding the detection chamber should be electropolished to reduce ^{222}Rn emanation. As should the diode be closer inspected on its emanation level since by now it contributes most to the background. We have no evidence of cosmic radiation induced background, but this hypothesis can be tested in the underground facility at MPIK.
To prevent water from freezing out on the cold plate, the carrier gas can be filtered through humidity traps. The collection efficiency of the cold plate could also be potentially improved with a lower temperature of the cold-plate. Cooling power could be gained by isolating the current cold-finger with mylar, to reduce infrared radiation loss. Another potential improvement

is to exchange the cold finger material with an even better heat conductor than copper. Heat pipes for example are known to have far better thermal properties than copper.

For the planning of an improved setup the COMSOL simulation might be helpful. From the temperature measurements it could be verified that the COMSOL simulations results are compatible with the thermal properties of the cold finger. The time until the cold plate reaches radon's freezing temperature of -71°C after start of cooling, COMSOL determined to be $\sim$8 minutes and tests to be $\sim$6 minutes. With this in mind this simple simulation is sufficient to plan a new improved Cryo Monitor.

Overall the above mentioned improvements and further research will lead to a detector with an even better sensitivity, capable of being employed in low-background physics.

References

[1] Planck Collaboration et al. Planck 2013 results. I. Overview of products and scientific results. , 571:A1, November 2014. doi: 10.1051/0004-6361/201321529.

[2] E. Aprile et al. Dark Matter Search Results from a One Ton-Year Exposure of XENON1T. Phys. Rev. Lett., 121(11): 111302, 2018. doi: 10.1103/PhysRevLett.121.111302.

[3] F. Zwicky. Die Rotverschiebung von extragalaktischen Nebeln. Helvetica Physica Acta, 6:110–127, January 1933.

[4] F. Zwicky. On the Masses of Nebulae and of Clusters of Nebulae. , 86:217, October 1937. doi: 10.1086/143864.

[5] V. C. Rubin, Jr. Ford, W. K., and N. Thonnard. Rotational properties of 21 SC galaxies with a large range of luminosities and radii, from NGC 4605 (R=4kpc) to UGC 2885 (R=122kpc). , 238:471–487, June 1980. doi: 10.1086/158003.

[6] M. Kamionkowski. WIMP and Axion Dark Matter. In E. Gava, A. Masiero, K. S. Narain, S. Randjbar-Daemi, G. Senjanovic, A. Smirnov, and Q. Shafi, editors, High Energy Physics and Cosmology, 1997 Summer School, volume 14, page 394, January 1998.

[7] Kim Griest. The Search for the Dark Matter: WIMPs and MACHOs. In Carl W. Akerlof and Mark A. Srednicki, editors, Texas/PASCOS '92: Relativistic Astrophysics and Particle Cosmology, volume 688, page 390, January 1993. doi: 10.1111/j.1749-6632.1993.tb43912.x.

[8] P. Tisserand, L. Le Guillou, C. Afonso, J. N. Albert, J. Andersen, R. Ansari, É. Aubourg, P. Bareyre, J. P. Beaulieu, X. Charlot, and et al. Limits on the macho content of the galactic halo from the eros-2 survey of the magellanic clouds. Astronomy Astrophysics, 469(2):387–404, Apr 2007. ISSN 1432-0746. doi: 10.1051/0004-6361:20066017. URL http://dx.doi.org/10.1051/0004-6361:20066017.

[9] Stacy S. McGaugh. A tale of two paradigms: the mutual incommensurability of ΛCDM and MOND. Canadian Journal of Physics, 93(2):250–259, February 2015. doi: 10.1139/cjp-2014-0203.

[10] Jouni Suhonen. Dark-matter detector observes exotic nuclear decay. Nature, 568.

[11] Background-free search for neutrinoless double- decay of 76ge with gerda. Nature, 544(7648):47–52, Apr 2017. ISSN 1476-4687. doi: 10.1038/nature21717. URL http://dx.doi.org/10.1038/nature21717.

[12] Laboratori Nazionali del Gran Sasso. Overview. URL https://www.lngs.infn.it/en/lngs-overview.

[13] E. Aprile, J. Aalbers, F. Agostini, M. Alfonsi, L. Althueser, F.D. Amaro, V.C. Antochi, F. Arneodo, L. Baudis, B. Bauermeister, and et al. Xenon1t dark matter data analysis: Signal and background models and statistical inference. Physical Review D, 99(11), Jun 2019. ISSN 2470-0029. doi: 10.1103/physrevd.99.112009. URL http://dx.doi.org/10.1103/PhysRevD.99.112009.

[14] E. Aprile et al. Projected WIMP sensitivity of the XENONnT dark matter experiment. JCAP, 11:031, 2020. doi: 10.1088/1475-7516/2020/11/031.

[15] E. Aprile, J. Aalbers, F. Agostini, M. Alfonsi, L. Althueser, F.D. Amaro, V.C. Antochi, E. Angelino, J.R. Angevaare, F. Arneodo, and et al. Excess electronic recoil events in xenon1t. Physical Review D, 102(7), Oct 2020. ISSN 2470-0029. doi: 10.1103/physrevd.102.072004. URL http://dx.doi.org/10.1103/PhysRevD.102.072004.

[16] Bundesamt für Strahlenschutz. Radon. URL https://www.bfs.de/DE/themen/ion/umwelt/radon/radon_node.html.

[17] Laboratoire National Henri Becquerel. Disintegration energy and half life. URL http://http://www.nucleide.org/.

[18] E. Aprile et al. ^{222}Rn emanation measurements for the XENON1T experiment. Eur. Phys. J. C, 81(4):337, 2021. doi: 10.1140/epjc/s10052-020-08777-z.

[19] International Atomic Energy Agency Nuclear Data.

[20] Th. Heumann. Diffusion in Metallen. Springer.

[21] R.Y. Rubinstein. imulation and the Monte Carlo Method. S. Ed. John Wiley and Sons Inc. New York, 1981.

[22] G. Audi, F. G. Kondev, Meng Wang, W. J. Huang, and S. Naimi. The NUBASE2016 evaluation of nuclear properties. Chinese Physics C, 41(3):030001, March 2017. doi: 10.1088/1674-1137/41/3/030001.

[23] G. Zuzel and H. Simgen. High sensitivity radon emanation measurements. Applied Radiation and Isotopes, 67 (5):889–893, 2009. ISSN 0969-8043. doi: https://doi.org/10.1016/j.apradiso.2009.01.052. URL https://www.sciencedirect.com/science/article/pii/S0969804309000608. 5th International Conference on Radionuclide Metrology - Low-Level Radioactivity Measurement Techniques ICRM-LLRMT'08.

[24] R. Wink, P. Anselmann, D. Dörflinger, W. Hampel, G. Heusser, T. Kirsten, P. Mögel, E. Pernicka, R. Plaga, and C. Schlosser. The miniaturized proportional counter HD-2(Fe)/(Si) for the GALLEX solar neutrino experiment. Nuclear Instruments and Methods in Physics Research A, 329(3):541–550, June 1993. doi: 10.1016/0168-9002(93)91289-Y.

[25] "Mitsuda et al.". Development of super-high sensitivity radon detector for the Super-Kamiokande detector. Nucl. Instrum. Meth., 2003.

[26] F. et al." "Mamedov. Development of an ultra-sensitive radon detector for the Super NEMO experiment. JINST, 2011.

[27] P.K. Hopke. . Health Phys., 57:39, 1989.

[28] J. Kiko. Detector for 222rn measurements in air at the 1mbq/m3 level. Nuclear Instruments and Methods in Physics Research Section A: Accelerators, Spectrometers, Detectors and Associated Equipment, 460(2):272–277, 2001. ISSN 0168-9002. doi: https://doi.org/10.1016/S0168-9002(00)01082-2. URL https://www.sciencedirect.com/science/article/pii/S0168900200010822.

[29] Werner G.Baechler. Cryopumps for research and industry. Vacuum, 37(1):21, 1987. doi: 10.1016/0042-207X(87)90078-9.

[30] Zuzel, G. Wojcik, M. A high-sensitivity large volume cryogenic detector for radon in gas. Journal of Radioanalytical and Nuclear Chemistry, 277, 2008. doi: 10.1007/s10967-008-0730-7.

[31] Vincent Baglin. Cryopumping and Vacuum Systems. CERN Accelerator School: Vacuum for Particle Accelerators, 2017.

[32] Pfeiffer Vacuum. Company website, . URL https://www.pfeiffer-vacuum.com/.

[33] Greisinger. Company website. URL hhttps://www.greisinger.de/.

[34] Pfeiffer Vacuum. Data sheet pkr 251, . URL https://static.pfeiffer-vacuum.com/productPdfs/PTR26002.en.pdf.

[35] FLIR. Company website. URL https://www.flir.de.

[36] Swagelok. Company website. URL https://www.swagelok.com/.

[37] Pfeiffer Vacuum. Data sheet hi pace 80, . URL https://static.pfeiffer-vacuum.com/productPdfs/PMP03941.en.pdf.

[38] G. Eurin, F. Joerg, and H. Simgen. Production and characterization of a ^{226}Ra implanted stainless steel radon source. (in preparation).

[39] G. Heusser et al. GIOVE - A New Detector Setup for High Sensitivity Germanium Spectroscopy At Shallow Depth. Eur. Phys. J. C, 75:531, 2015.

[40] James Cox. Fundamentals of Linear Electronics: Integrated and Discrete. Delmar Thomson Learning.

[41] Hamamatsu. Company website, . URL https://www.hamamatsu.com/eu/en/index.html.

[42] Hamamatsu. Data sheet si pin photodiode, . URL https://www.hamamatsu.com/eu/en/product/type/S3204-08/index.html.

[43] Fast ComTec. Company website, . URL https://www.fastcomtec.com/.

[44] Fast ComTec. Data sheet multichannel analyzer, . URL https://www.fastcomtec.com/fwww/datashee/mcd/mca-3.pdf.

[45] COMSOL. Company website. URL https://www.comsol.de.

[46] H. Balsiger M. Hässig A. Jäckel P. Wurz B. Fiethe M. Rubin S. A. Fuselier J. J. Berthelier J. De Keyser H. Rème U. Mall B. Schläppi, K. Altwegg. Influence of spacecraft outgassing on the exploration of tenuous atmospheres with in situ mass spectrometry. Space Physics - Journal of Geophysical Research, 115(A12), 2017.

A Cryogenic Monitor Technical drawing

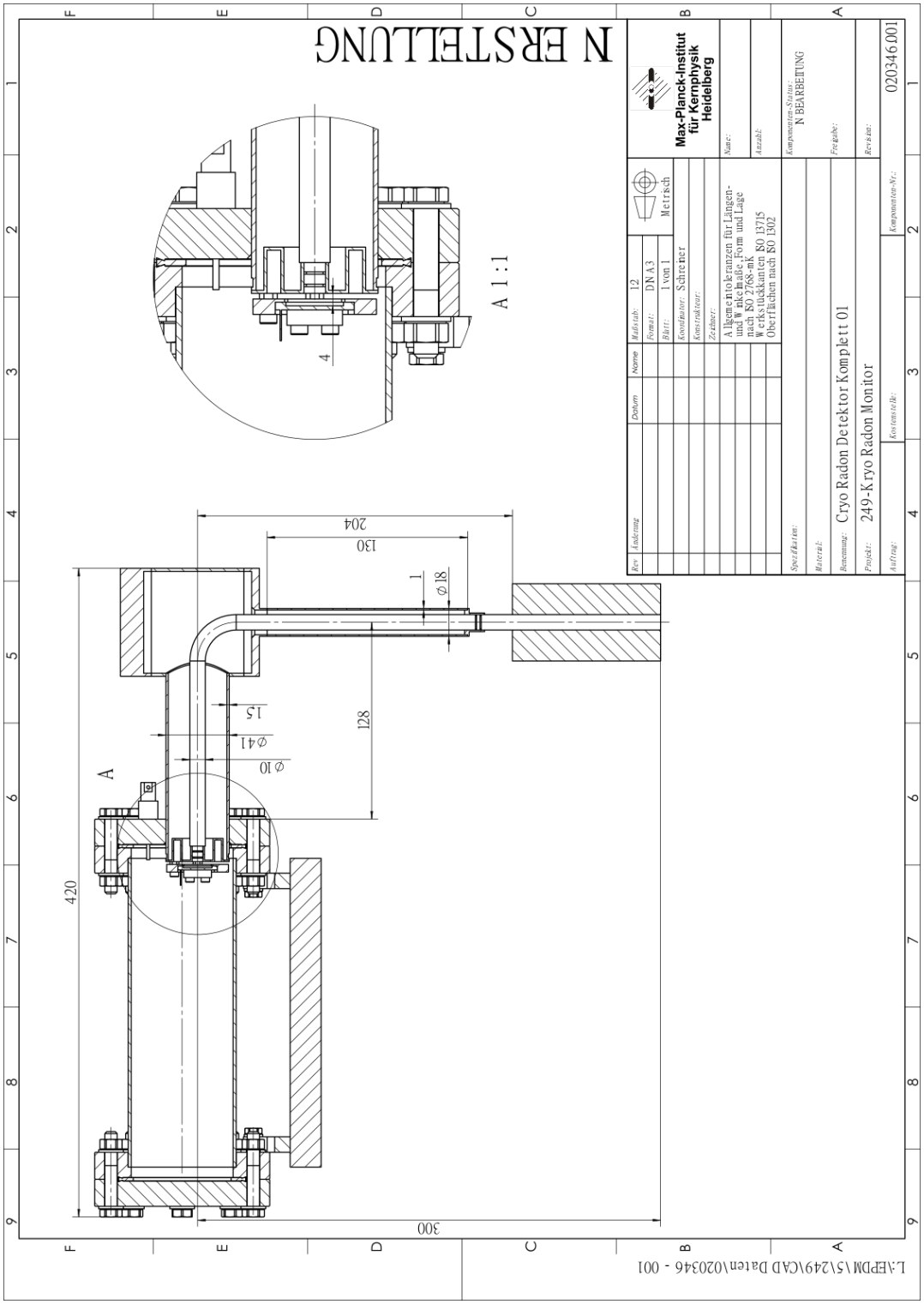

Figure A.1: Design of the Radon Monitor at MPIK

List of Figures

List of Tables

Acknowledgement

I would like to thank everyone who made this bachelor thesis possible. First, I like to thank Prof. Manfred Lindner for giving me the opportunity to do my thesis in the XENON group at MPIK. I like to thank Jochen Schreiner for giving me his Cryo Monitor setup for my bachelor thesis and supporting me in my first steps.

Moreover, I like to thank Hardy Simgen for his advice in helping me to correct my thesis and his overall support in commissioning the Cryo Monitor. His guidance during my work and the numerous tips for improving my thesis were of great value to me. He patiently answered all my questions and gave me new ideas for my work.

Furthermore, I thank every group member for providing a welcoming atmosphere, helping me with all my problems and taking time to answer my questions. Special thanks go to Florian Joerg for helping me in the COMSOL simulation and Theresa Marrodán for giving me feedback on my thesis.

Last but not least, I want to express my utmost gratitude towards Joaquim Palacio for his patience, his kindness and his overall support in my bachelor thesis. Even on his vacation he still provided me with feedback for my bachelor thesis and overall advice in his daily telephone calls. I cannot imagine having a better tutor than him. Thank you, Quim.